Models and Tools for Heat Transfer, Thermal Stresses and Stability of Composite Aerospace Structures

by
R. Rolfes,. J. Teßmer, K. Rohwer
DLR, Institute of Structural Mechanics,
Lilienthalplatz 7, D-38108 Braunschweig, Germany

1. Introduction

2. Heat Transfer in Hybrid Composite Shells
2.1 Layerwise Thermal Lamination Theories and Finite Elements
2.2 Realistic Boundary Conditions for Starting Aircraft
2.3 Application to Fiber Metal Laminates for Aircraft Structures

3. Thermally Induced Stresses in Composite Shells
3.1 Extended 2D Method for Transverse Thermal Stresses based on FSDT
3.2 Higher Order Theories
3.3 Thermally Induced Buckling

Running Title: Models and Tools for Composite Aerospace Structures

Abstract:

An overview of DLR´s current research activities and results in the fields of heat transfer, thermal stresses and thermally induced buckling in composite aerospace structures is given. Novel theories and finite element formulations are presented, realistic modelling of boundary conditions and junction areas is highlighted, experimental validation is discussed, and finally design guidelines are given.

Keywords: Composites, Hybrid Structures, Fiber Metal Laminates, Heat Transfer, Thermal Stresses, Thermal Buckling

1. Introduction

The present paper gives an overview of current research activities and results which were gathered in fundamental research projects on composite analysis as a co-operation between DLR and NASA Langley, in DLR internal multidisciplinary research projects on reentry, on European future launcher projects, and in National future large aircraft projects. Consequently, primary applications are for reentry vehicles, e.g. hot structures, thermally protected warm structures, cryogenic tanks, and for aircraft structures, e.g. primary structures like wing, fuselage, flaps, stabilizers of transonic and supersonic commercial aircraft. The focus is on composite and hybrid composite lightweight structures. Efficient shell analysis and design considerations for representative structural components like stringer stiffened panels are within the central scope of the paper.

In chapter 2 heat transfer is dealt with. After outlining efficient theories and finite element formulations for hybrid composite structures the major problem of representing realistic thermal boundary conditions is discussed. Suggestions are made which are then applied to a CFRP and a fiber metal structure.

Also chapter 3 starts with novel theories. Here, the emphasis is on an efficient procedure to determine 3D thermal stresses as a prerequisite for reliable failure prediction by use of 3D failure criteria. After discussing the simple and easily applicable extended 2D-method, limitations of the theory especially for prediction of transverse normal stresses are investigated and suggestions for improvement are made. The chapter closes with design rules for stringer-stiffened panels under combined thermo-mechanical loading. Design and optimization suggestions for practical application are made.

2. Heat Transfer in Hybrid Composite Shells

Composite materials like carbon fiber reinforced plastics (CFRP) or fiber metal laminates (FML) are increasingly used for primary components of commercial aircraft. Various configurations like monolithic or sandwich constructions can possibly be made of composite materials. Thermal loads, mainly consisting of solar radiation are comparatively low. However, the thermal analysis has to certify that the maximum temperature is kept well below the glass transition temperature of the resin. Experimental and numerical tests in the past have pointed out that valid design rules are often too conservative. Therefore, to be efficient, there is a need to find more realistic thermal loads, thermal boundary conditions and improved thermal analysis tools for future composite aircraft structures. Chapter 2.1 deals with the development of accurate and fast analysis tools. Since common analysis codes and algorithms mainly focus on classical metallic aircraft components, these methods and tools have to be customized and validated for all composite aircraft structures. This is even more important as primary load bearing substructures will be made of composite materials. Another point of interest are new and more efficient numerical analysis methods. Therefore, 2D- finite element formulations are developed, since experiences show that 3D-modeling is very time consuming and data exchange to stress analysis models (usually 2D-models) is difficult. The second crucial aspect, the determination of realistic thermal conditions and loads, is addressed in chapter 2.2. Maximum temperatures at moments with critical mechanical stresses heavily depend on accurate boundary conditions and modeling. The influence of different colors and intensity of convection are only two factors to be mentioned within this context. Chapter 2.3 is concerned with the application of the newly developed methods and finite elements to aircraft structures out of CFRP and Fiber Metal Laminates.

2.1 Layerwise Thermal Lamination Theories and Finite Elements

Today the thermal analysis of aerospace structures is frequently carried out by use of the finite difference method (FDM). P/THERMAL, IDEAS-TMG, SINDA or ESATAN are examples of commercial programmes based on FDM. However, this method has some shortcomings, especially if applied to composite structures. Originally, it was designed for radiation dominated problems (e.g. satellites). It is faced with severe problems, if heat conduction plays the major role, since there is no general procedure for calculating the conduction resistors. Even greater problems arise with anisotropic materials (like CFRP). One drawback is, that the lamination theory for heat conduction can't be introduced into this method. Another problem arises from inhomogenity (CFRP is built up from different layers, other composites like FML consist additionally of different materials).

Growing interest is focused on the Finite Element Method (FEM), which allows to use standard 3D finite elements or special 2D elements, based on the lamination theories. For the modeling of aircraft composite structures the FEM is strongly recommended in case of thermal analyses. This method not only provides special elements, but also avoids the modeling uncertainties of the FDM and eventually allows to use the same model in both, thermal and mechanical analysis. Nevertheless it should be mentioned that the FDM has been successfully applied by many users. They have gathered broad experience in skilful modeling, which can sometimes help to overcome the problem of uncertain conduction resistors.

One main objective of the thermal analysis is to certify that a structure fulfils the thermal requirements and to supply the full three-dimensional temperature distribution as input for the thermo-mechanical analysis. In the case of monolithic and hybrid composites, like sandwich structures or fiber metal laminates, the layers have different thermal conductivities in different directions. Figure 1 shows examples of different composites.

In general, finite element thermal analyses are performed using 3D elements of commercially available tools. With these elements problems arise due to high computational effort and coupling of thermal and mechanical analyses.

2D finite elements overcome these problems. Besides, for thermo-mechanical calculations of thin-walled structures a two-dimensional model is generally sufficient. Most commercial finite element codes provide two-dimensional finite elements for composite and sandwich structures. Therefore it is desirable to have finite elements, based on a two-dimensional model, which are able to determine the full three-dimensional temperature distribution. Therewith the modeling and numerical effort would be drastically reduced. For laminated composites (CFRP) Rolfes [2] has proposed a linear thermal lamination theory which is analogous to the first order shear deformation theory (FSDT). However, for local effects the heat flux calculated from the derivatives of the temperature field is not well approximated. Moreover the linear temperature distribution over the thickness might be too rough in the case of transient heat conduction. To overcome these shortcomings a higher order quadratic thermal lamination theory and associated finite elements have been developed by the same author [7]. Other approaches for multilayered composites are described by Agyris et al. [1] and Noor et al. [5].

Subsequently, new 2D finite element formulations are outlined which are based on layer-wise linear or quadratic temperature distributions in thickness direction. This allows to analyze composite structures with different thermal conductivity in thickness direction for each layer.

These elements can also be used for lightweight structures in very cold or very hot environments where layers of load bearing material and isolations with different thermal and stiffness properties are combined in one lay-up. It should be mentioned that the finite element formulations are well suited for to be used in a concurrent integrated engineering process. Due to the two-dimensional data structure of the thermal model it can be coupled much easier to mechanical models consisting of shell elements than conventional three-dimensional thermal models. This is important for fast and accurate analysis within the preliminary design phase of structural parts.

2.1.1 Formulation

CFRP, hybrid composites and sandwich structures can be idealized as layered structures, see Figure 2. For layers in which all modes of heat transfer (heat conduction, radiation and convection) occur (for example honeycomb cores) a thermal homogenization is necessary. This homogenization is not a specific requirement for 2D finite elements, but is equally needed if a 3D finite element or finite difference model is applied. A layerwise discretisation with 3D finite elements is very costly. Therefore different approaches have been proposed to reduce the modeling effort. For an overview of these approaches see [4], [6] and [8]. The thermal lamination theory (TLT) as developed by Rolfes [2,7] has proven a useful method for CFRP structures. It assumes either linear or quadratic temperature distributions over the whole laminate thickness. This theory holds under the following conditions:

- Identical thermal conductivity of all layers in the thickness direction
- No heat-transfer resistance at the interfaces

The linear TLT can then be formulated as

$$T(x,y,z) = T_0^{(b)}(x,y) + z \cdot T_{0,z}^{(b)}(x,y). \tag{1}$$

Non-linear temperature distributions in thickness direction can occur in case of

- large temperature gradients in the thickness direction in conjunction with temperature-dependent thermo-physical properties
- transient problems with rapid heating
- spatially concentrated thermal loads

In such cases, the quadratic TLT is better suited. It assumes

$$T(x,y,z) = T_0^{(b)}(x,y) + z \cdot T_{0,z}^{(b)}(x,y) + \frac{z^2}{2} T_{0,zz}^{(b)}(x,y). \tag{2}$$

For modeling hybrid structures (e.g. metallic multiwall TPS, hybrid composites like fiber metal laminates, sandwiches or hot structures) it is necessary to abandon the first condition stated above, and to replace it by the assumption of

- different thermal conductivity of each layer in thickness direction.

This leads to the need of layerwise theories.

A linear layered theory (LLT) (conf. Figure 2) was first used by Sipetov [9] for steady state thermal problems. It assumes for each layer k

$$T^{(k)}(x,y,z) = T_0^{(k)}(x,y) + z_k \cdot T_{0,z}^{(k)}(x,y) .$$
(3)

Using two heat transfer equilibrium conditions at each layer interface for the

- temperature and the
- heat flux in transverse direction

the number of functional degrees of freedom can be made independent from the number of layers. This theory was extended to transient problems by Noack and Rolfes [3].

For the same reasons as stated for the TLT, a quadratic layered theory was formulated for transient thermal problems and local heat loads. It reads

$$T^{(k)}(x,y,z) = T_0^{(k)}(x,y) + z_k \cdot T_{0,z}^{(k)}(x,y) + \frac{z_k^2}{2} T_{0,zz}^{(k)}(x,y) .$$
(4)

By using of a third heat transfer equilibrium condition at each layer interface for

- the change of the heat flux in transverse direction,

again the number of functional degrees of freedom can be made independent from the number of layers. This third heat transfer condition is chosen as $q_{z,z}^{(k)} = q_{z,z}^{(k+1)} = const.$ While this seems to be mathematically stringent, there is physically no justification for this interface condition. Alternatively, also $T_{,zz}^{(k)} = T_{,zz}^{(k+1)} = const.$ could be chosen. However, numerical examples have shown that the former assumption provides very reasonable results. Based on these theories the finite elements QUADLLT and QUADQLT were developed, showing linear or quadratic temperature distributions in thickness direction for each layer.

Starting with Fourier's law for layer k of anisotropic material

$$\underset{\sim}{q}^{(k)} = -\underset{\sim}{K}^{(k)} \cdot (\text{grad}\, T)^{(k)}$$
(5)

equations (3) and (4) may alternatively be used for the approximation of the temperature T. Introducing the above mentioned heat transfer equilibrium conditions at the layer interfaces leads to

$$T^{(k)}(x,y,z) = T_0^{(b)}(x,y) + \tilde{z}_k(z) \cdot T_{0,z}^{(b)}(x,y)$$
(6)

for the linear layerwise approximation and

$$T^{(k)}(x,y,z) = T_0^{(b)}(x,y) + \tilde{z}_k(z) \cdot T_{0,z}^{(b)}(x,y) + \tilde{\tilde{z}}_k(z,z^2) \cdot T_{0,zz}^{(b)}(x,y)$$
(7)

for the quadratic layerwise approximation. The index b denotes the reference layer. The values of $\tilde{z}_k$ and $\tilde{\tilde{z}}_k$, which are functions of the thickness-coordinate z, are specified in

references [3] and [4]. It should be emphasized that for both formulations the functional degrees of freedom remain independent of the number of layers which is crucial for a computational efficiency.

Introducing these equations into the three-dimensional weak formulation for linear steady-state heat transfer

$$\int_\Omega (\text{grad}\, v)^T \underset{\sim}{K}\, \text{grad}\, T\, \mathrm{d}\Omega + \int_\Gamma \underset{\sim}{q}^T \underset{\sim}{n}\, v\, \mathrm{d}\Gamma = 0 \qquad (8)$$

allows to separate the integration in z-direction from the integration in x- and y-direction. Performing the integration in z-direction analytically, the finite element method can be applied to the remaining two-dimensional weak formulation

$$\int_A \underset{\sim}{N}^T \underset{\sim}{\tilde{K}} \underset{\sim}{N}\, \vartheta\, \mathrm{d}A + \int_\Gamma \underset{\sim}{q}^T \underset{\sim}{n}\, v\, \mathrm{d}\Gamma = 0 \,. \qquad (9)$$

In equation (8) v is the test function. The boundary conditions at the edge Γ, considering free convection q_c and heat flux $\bar{q}$, read

$$\underset{\sim}{q}^T \underset{\sim}{n} = q_c + \bar{q} \,. \qquad (10)$$

The integration in z-direction leads to the modified heat conduction matrix $\underset{\sim}{\tilde{K}}$. The shape functions and their derivatives are summarized in the matrix $\underset{\sim}{\tilde{N}}$ and the nodal degrees of freedom in the vector ϑ. Equation (9) can now be implemented into an ordinary 2D finite element formulation. A full elaboration with detailed presentation of all matrices is shown in [3] and [4].

2.1.2 Examples

A square plate with a local heat flux of q = 100 kW/m^2 is considered. Besides adiabatic conditions are assumed at the upper surface. At the bottom of the plate and on the edges a convection boundary condition with an ambient temperature of
T$_\infty$ = 0 °C and α_c = 30 W/m^{2}K is applied. The geometry is shown in Figure 3.

Two different configurations are studied, a sandwich and a hybrid composite plate. The sandwich has two facings with three layers each and a honeycomb core. The hybrid composite CARE is a fiber metal laminate made up from aluminum and CFRP. The steady state temperature distributions in transverse direction at point P are shown in Figure 4. It shows comparisons of both new elements with a full 3D analysis using HEXA elements of MSC.NASTRAN. The results show a good agreement between 2D and 3D analysis. Especially, quadratic layered theory and 3D results match excellently. It is clearly visible that QUADQLT is very well capable of describing this phenomenon whereas QUADLLT shows slight deviations. It should be kept in mind that strongly concentrated heat flux is a rather tough test for the elements. In many applications the thermal loading will be much more uniform and the temperature distribution can be kept properly already by the linear element. Numerical and modeling effort are drastically reduced by the new finite elements.

2.2 Realistic Boundary Conditions for Starting Aircraft

Using fiber composite epoxy for primary aircraft structures has brought about the question of thermal effects during the starting phase. Of major concern is that under elevated temperatures, composites with epoxy resin may encounter fractions which would result in a reduction of stiffness and strength properties. In contrast to classical metallic materials this reduction starts at temperatures which could already be reached under realistic hot environmental conditions. Since dimensioning load cases appear shortly after take-off, the knowledge of the temperature field within the primary load bearing structure is necessary for an accurate failure analysis.

A major problem for an accurate thermal analysis of a starting aircraft is the determination of realistic boundary conditions. In this context on one hand radiation loads must be determined, as resulting from direct and reflected solar radiation as well as from thermal radiation of the ground, of surrounding structures or of the atmosphere. On the other hand, convective loads have to be considered. Therefore, realistic convective coefficients must be specified for natural and forced convective heat transfer.

For the steady state case (e.g. parking on ground) the structural temperature field is influenced by:
- ambient conditions (solar flux, air temperature, ground temperature, ground emission and absorption coefficients, air velocity)
- layout (contour) of the structure
- structural heat conduction properties

Additionally, for the transient (unsteady) case, the structural heat capacity has to be regarded.

Main drivers for heat transfer are:
- solar radiation absorption
- radiation between structure and ground
- radiation between different structural zones
- radiation between structure and sky atmosphere
- convection between structure and atmosphere

Solar Radiation Absorption : Regarding hot environmental conditions, the amount of heat induced by solar radiation can be estimated easily. Assuming clear skies, the solar heat intensity (≈ 1000 W/m^2, depending on height) is well known. Beside direct solar radiation, also reflection of ground or other structures have to be taken into account. Important parameters are the solar absorption coefficient α_s of the aircraft structure and the solar reflection coefficient $\rho_s = 1 - \alpha_s$ of the ground. Both can vary heavily and have to be determined properly. Under conservative assumptions a structural and ground absorption of α_s=1.0 combined with a hot ground surface temperature of T$_{ground}$= 80°C could be chosen.

Radiation between Structure and Ground: In addition to reflected solar radiation, the ground has also to be taken into account for thermal radiation between the structure and the ground surface itself. For this thermal radiation thermal absorption coefficients α_{th} have to be provided for the structure and the ground. Usually, a very hot ground temperature of

T$_{ground}$ = 80°C in combination with a high thermal absorption of 0.9, which implies a very dark surface, is assumed.

Radiation between different Structural Zones: Inter-structural radiation has to be regarded at places where different structural zones have considerable view factors to each other. This implies only for special substructures. For larger components like wing or fuselage this influence is of minor relevance.

Radiation between Structure and Sky Atmosphere: With a considerable influence on the structural temperature field, radiation between the structure and the surrounding sky atmosphere has to be computed. An easy equation for a representative temperature of the sky atmosphere is given by Swinbank [10], with

$$T_{\text{sky}} = 0.0552 \cdot T_{\text{amb}}^{1.5}, \tag{11}$$

where the sky temperature T_{sky} and the ambient air temperature T_{amb} are given in Kelvin. Disadvantages of this approach appear at higher temperatures over 40°C, when unrealistic high values are computed. Another presentation, given by Idso & Jackson, see [11], with

$$T_{\text{sky}} = 1 - 0.261 \cdot \exp[-0.000777 \cdot (273 - T_{\text{amb}})^2], \tag{12}$$

is quite similar but realistically remains with $T_{sky} < T_{amb}$ for higher temperatures.

Convection between Structure and Atmosphere: Forced convection is the main process, responsible for cooling down after the aircraft starts moving. With a given wind speed profile, the heat transfer coefficient for forced convection h can be determined.
The equation

$$\text{Nu}(x) = 0,0296 \cdot \text{Re}^{4/5} \cdot \text{Pr}^{1/3} \tag{13}$$

provides the local Nusselt (Nu) number as function of Reynolds (Re) and Prandtl (Pr) numbers for turbulent conditions. Finally, the forced convection

$$h = \text{Nu} \cdot \lambda / x \tag{14}$$

can be approximated by the Nusselt number, the thermal conductivity λ and the position x within the length of the thermal boundary layer. Natural convection, which may cause a realistic heat transfer coefficient up to approximately 3 W/m^{2}K, is taken into account by assuming a minimum wind speed of 2m/s. As it can be seen by formulae (13) and (14) the heat transfer coefficient depends mainly on two parameters, one is the air flow velocity, the other is the position within the boundary layer of the structure. Figure 6 shows two curves for positions at $x = 1.0m$ (typical for wing dimensions) and $x = 50.0m$ (typical for fuselage dimensions). The differences are obvious. The kink within the curve for $x = 1.0m$ results from the laminar-turbulent transition, where for $x = 50.0m$ only the turbulent region is relevant.

As pointed out the air flow velocity is one major factor for cooling during the take off. Figure 7 shows a typical profile of the air flow velocity over time.

By evaluating equations (13) and (14) the air flow velocity can be transformed into a function for the heat transfer coefficient, see Figure 8. In this case a mean value is calculated for a structural length of $L = 4,0m$.

Another important and parameter, also varying with time, is the ambient air temperature which depends on the assumed ground temperature and the actual height of the aircraft. Such an exemplary temperature profile is given in Figure 9. The described profile is derived by a combination of an ISA-temperature function (temperature as function of hight) with an appropriate take off scenario (hight as function of time).

With these input parameters for forced convection the partial heat flux

$$q(h) = h(T_{struct} - T_{amb})$$

(15)

can be computed within the numerical analysis.

2.3 Application to CFRP and Fiber Metal Laminates

As composite materials become more and more common for primary aircraft structures, the thermal analysis plays a growing role for the design process. A typical part which could be made of composite in future aircraft is a CFRP wing box, shown in Figure 10.
Main points for thermal evaluation are shown in Figure 11.

Conducting a steady state analysis, the effect of a varying solar absorption coefficient α_s is shown in Figure 12. It comes out very clearly, that a painting with a low α_s and high thermal emissivity ε_{th} has a favorable influence on the temperature in the sense of limited heating.

The influence of a varying heat convection factor is shown in Figure 13, where the strong influence of this parameter is pointed out. Values are computed for a steady state case which is relevant for a parking scenario on ground.
Taking a heat transfer coefficient of 8 W/m^2, a thermal emissivity and solar absorptivity of 0.9, the transient heating on hot environmental conditions up to a steady state limit (after approximately 1 hour) for a CFRP wing box is presented in Figure 14.
Then taking into account a take off scenario, described in chapter 2.2, the cooling of the structure is shown in Figure 15.
Taking the steady state values as starting condition, a little drop of temperatures is observed during taxiing. Then, by having a one minute stop, the structure heats up again. During the following take off a rapid cooling is visible.

For fuselage structures fiber metal laminates exhibit new potential weight savings. As for other composites, they also show a drop of strength and stiffness for hot temperatures. Therefore, accurate thermal analyses are necessary. An exemplary cross section, Fig. 16, was discretised with panels, shown in Fig. 17.
For such structure a similar computation of the temperature field as for the wing box was conducted. A crucial point is the validation of the numerical model of the panel. Therefore, experimental tests were carried out at the DLR THERMEX test facilities.
These tests were compared to numerical computations on panel level. Typical contour plots are shown in Figure 18. In this manner it is possible to compute temperature fields for various composite aircraft substructures. This gives an accurate basis for all mechanical computations, where temperature effects have to be taken into account.

3. Thermally Induced Stresses in Composite Shells
3.1 Extended 2D Method for Transverse Thermal Stresses based on FSDT

When a shell or plate is subjected to a temperature change, the distribution of which can be calculated by the methods described in chapter 2, thermal strains are generated if the thermal expansion coefficient is unequal to zero. Thermally induced stresses do only appear if the free deformation of the structure is restrained either by internal constraints or by external boundary conditions. In-plane stresses can occur as well as transverse stresses.

In case of a uniform thermal load within the x_1-x_2-plane transverse stresses can only develop near the boundaries. At free edges the transverse shear resultant must vanish, however, interlaminar shear eigen-stresses are normally present since the thermal expansion behavior changes from layer to layer. Transverse shear resultants can develop at supported boundaries if the thermal load causes bending of the plate. This occurs in symmetric laminates under non-symmetric temperature distribution in thickness direction, or in unsymmetrical laminates even under uniform through-the-thickness temperature. In case of non-uniform thermal loading within the x_1-x_2-plane, thermally induced transverse stresses can occur throughout the whole plate. The importance of transverse stresses for predicting the onset of damage in composites is widely accepted. Consequently, modern failure criteria account for the full stress tensor even for applications to thin-walled structures [12].Therefore an efficient method for predicting thermally induced transverse stresses is required.

The first order shear deformation theory (FSDT) has proven to be a good compromise between low effort and high accuracy. Generally, good results are achieved for displacements and in-plane stresses whereas transverse stresses show poor quality when calculated using the material law. If the three-dimensional equilibrium conditions are used instead then realistic transverse stress distributions can be achieved at least under mechanical loading. This procedure has already been proposed by Pryor and Barker [13]. However, their method needs fourth order shape functions in order to evaluate all derivatives required on element level. The extended 2D-method of Rolfes and Rohwer [14] which bases on simplifying assumptions needs only quadratic shape functions. This allows elementwise evaluation of derivatives in 8 or 9 noded elements. The extension of this method to thermal loading is discussed subsequently. The content is primarily based on the publications [15, 8].

The 3D-equilibrium conditions write

$$\sigma_{\alpha 3,3} + \sigma_{\alpha \beta,\beta} = 0 \qquad\qquad (16)$$
$$\sigma_{33,3} + \sigma_{\alpha 3,3} = 0 \qquad\qquad (17)$$

where equations (16) are used to compute the transverse shear stresses $\sigma_{\alpha 3}$ from the in-plane stresses $\sigma_{\alpha \beta}$. The components of $\sigma_{\alpha \beta}$ are written in vector form and denoted as $\underset{\sim}{\sigma}_m$. For the FSDT they read

$$\underset{\sim}{\sigma}_m = \underset{\sim}{\tilde{C}} \,(\underset{\sim}{\varepsilon}^\circ + x_3 \underset{\sim}{\kappa} - \underset{\sim}{\alpha} \Delta T)\,, \qquad\qquad (18)$$

where $\underset{\sim}{\varepsilon}^\circ$, $\underset{\sim}{\kappa}$ and $\underset{\sim}{\alpha}$ are extensional strains and curvatures of the reference surface and coefficients of thermal expansion, respectively. $\underset{\sim}{\varepsilon}^{(\circ)}$ and $\underset{\sim}{\kappa}$ can be expressed by the in-plane

and bending stress resultants $\underset{\sim}{N}, \underset{\sim}{N}^{th}, \underset{\sim}{M}$ and $\underset{\sim}{M}^{th}$ when using the thermo-elastic constitutive relation for the laminate

$$\begin{bmatrix} \underset{\sim}{\varepsilon}^{\circ} \\ \underset{\sim}{\kappa} \end{bmatrix} = \begin{bmatrix} \underset{\sim}{\tilde{A}} & \underset{\sim}{\tilde{B}} \\ \underset{\sim}{\tilde{B}} & \underset{\sim}{\tilde{D}} \end{bmatrix} \begin{bmatrix} \underset{\sim}{N} + \underset{\sim}{N}^{th} \\ \underset{\sim}{M} + \underset{\sim}{M}^{th} \end{bmatrix}$$

(19)

The matrices $\underset{\sim}{\tilde{A}}$, $\underset{\sim}{\tilde{B}}$, and $\underset{\sim}{\tilde{D}}$ are inverse matrices of the laminate's in-plane, coupling and bending stiffness matrices $\underset{\sim}{A}, \underset{\sim}{B}$ and $\underset{\sim}{D}$. Including eq.'s (17) and (18) into eq. (16) yields a formulation for the transverse shear stresses $\sigma_{\alpha 3}$ which depends on laminate matrices and first derivatives of the in-plane and bending stress resultants.

At this point two simplifying assumptions come into play. Firstly, the influence of the first derivatives of the in-plane stress resultants on the transverse shear forces is neglected and, secondly, the deformation behavior is approximated by two cylindrical bending modes. Thus, the following derivatives vanish

$$N_{,\alpha} = 0$$

(20)

$$M_{11,2} = M_{22,1} = M_{12,1} = M_{12,2} = 0$$

(21)

The remaining derivatives of the bending stress resultants can be expressed by the transverse shear resultants

$$M_{11,1} = R_1$$

(22)

$$M_{22,2} = R_2$$

(23)

by applying equilibrium. When introducing equations (17) to (20) into eq. (16) the final equation for the transverse stresses appears after some algebraic manipulations

$$\underset{\sim}{\tau} = \underset{\sim}{f} \underset{\sim}{R} + \underset{\sim}{B}_{\alpha} \left(\begin{bmatrix} \underset{\sim}{G} & \underset{\sim}{F} \end{bmatrix} \begin{bmatrix} \underset{\sim}{A}^{th} & \underset{\sim}{B}^{th} \\ \underset{\sim}{B}^{th} & \underset{\sim}{D}^{th} \end{bmatrix} + \begin{bmatrix} \underset{\sim}{a}^{th} & \underset{\sim}{b}^{th} \end{bmatrix} \right) \begin{bmatrix} T_{,\alpha\beta}^{(0)} \\ T_{,\alpha\beta}^{(1)} \end{bmatrix}$$

(24)

The matrices $\underset{\sim}{f}, \underset{\sim}{G}, \underset{\sim}{F}, \underset{\sim}{a}^{th}, \underset{\sim}{b}^{th}, \underset{\sim}{A}^{th}, \underset{\sim}{B}^{th}$ and $\underset{\sim}{D}^{th}$ only depend on the laminate properties and can easily be evaluated. (for more details see [8]). $\underset{\sim}{B}_{\alpha}$ are simple Boolean matrices, $T^{(0)}$ is the temperature of the reference surface and $T^{(1)}$ denotes the temperature gradient in thickness direction (linear distribution assumed). Applying the third equilibrium condition (17) allows for evaluating even the transverse normal stress. After some algebraic work it appears

$$\sigma_{33}(x_3) = -\underset{\sim}{b}_{\alpha} \underset{\sim}{f}^{*} \underset{\sim}{R}_{,\alpha} + \underset{\sim}{b}_{\alpha} \underset{\sim}{B}_{\beta} \left(\begin{bmatrix} \underset{\sim}{G}^{*} & \underset{\sim}{F}^{*} \end{bmatrix} \begin{bmatrix} \underset{\sim}{A}^{th} & \underset{\sim}{B}^{th} \\ \underset{\sim}{B}^{th} & \underset{\sim}{D}^{th} \end{bmatrix} + \begin{bmatrix} \underset{\sim}{a}^{*th} & \underset{\sim}{b}^{*th} \end{bmatrix} \right) \begin{bmatrix} T_{,\alpha\beta}^{(0)} \\ T_{,\alpha\beta}^{(1)} \end{bmatrix}$$

(25)

The superscript $*$ denotes integration in thickness direction up to x_3. The extended 2D-method can easily be implemented into a pre- and postprocessing software tool for any finite element code which comprises a shell element based on the FSDT. By that means the full 3D state-of-

stress is evaluated by using a standard shell discretisation and performing a very rapid postprocessing.

The performance and limitations of the extended 2D-method are illustrated by the subsequent examples. A simply supported plate with anti-symmetric stacking [0/90/0/90] was subjected to static and temperature loading. The latter one was either uniform in thickness direction or linear. Material properties typical for CFRP with high tenacity fibers were chosen.

$$E_1/E_2 = 15; \; G_{12}/E_2 = 0.5; \; G_{22}/E_2 = 0.3378; \; \nu_{12} = 0.3; \; \alpha_1 = 0.139*10^{-6}; \; \alpha_2 = 9.0*10^{-6}$$

Figure 19 shows transverse shear stress distributions which are compared to an analytical 3D solution, denoted as "exact", and an equilibrium method without simplifying assumptions, denoted as "3D Post Processing". In general the approximation of the extended 2D-method is good, often very good. The full equilibrium approach provided even better results, however, one should keep in mind that it requires higher order derivatives which can usually not be evaluated in finite element computations on element level. While the transverse shear stresses are already small compared to the in-plane stresses, the transverse normal stress is even much smaller than the transverse shear stresses.

Figure 20 shows the results for two aspect ratios of the plate. For mechanical loading the results are excellent, for thermal gradient loading they are at least good. However, under a temperature load which is uniformly distributed through the thickness the results are poor for the plate with aspect ratio 1. In this case the maximum transverse normal stress is only $2.5\,^0/_{00}$ of the maximum transverse shear stress. It is interesting to notice that the application of the full equilibrium method does not improve the results. This gives rise to the assumption that in these cases the FSDT finds its limitations. This problem can be resolved by applying higher order theories as will be shown in the following.

3.2 Higher Order Theorie

3.2.1 Conditional need for higher order theories

From the explanations and examples given above it is obvious that the extended 2D method based on the First Order Shear Deformation Theory (FSDT) delivers thermally induced stresses which in many cases compare very well with those obtained by means of the much more expensive 3D analysis. That holds especially for the transverse shear stresses; in a few cases transverse normal stresses, however, deviate considerably from the exact solution. In the following, reasons for these discrepancies are investigated more closely.

Test cases are rectangular plates where the boundary conditions

$$u_2 = 0, \quad w = 0, \quad \varphi_2 = 0, \quad \sigma_{11} = 0 \quad \text{at} \quad x_1 = 0, L_1$$
$$u_1 = 0, \quad w = 0, \quad \varphi_1 = 0, \quad \sigma_{22} = 0 \quad \text{at} \quad x_2 = 0, L_2 \tag{26}$$

are enforced along the edges. The quantities φ_1 and φ_2 specify the normal rotation around the axes x_2 and x_1 respectively. The plates consist of layered fiber composites the material properties of which are assumed as

$$E_L / E_T = 15, \quad G_{LT} / E_T = 0.5, \quad G_{TT} / E_T = 0.3378, \quad \nu_{LT} = 0.3,$$
$$\nu_{TT} = 0.48, \quad E_T = 10.0 \text{ GPa}, \quad \alpha_L = 0.139 \cdot 10^{-6} K^{-1}, \quad \alpha_T = 9 \cdot 10^{-6} K^{-1} \tag{27}$$

Discrepancies in the resulting stresses appear for example if the plates are loaded by a temperature distribution of the form

$$\Delta T(x_1, x_2, x_3) = \overline{T}_0 \sin(\pi x_1 / L_1) \sin(\pi x_2 / L_2) + x_3 \overline{\overline{T}}_1 \sin(\pi x_1 / L_1) \sin(\pi x_2 / L_2) \tag{28}$$

Rolfes et al. [15] have shown that for all cases considered, the transverse shear stresses at the edge half way between two corners obtained by means of the extended 2D method compare very well with the corresponding 3D results. Transverse normal stresses at the plate center, however, are in many cases not well determined by the extended 2D method. That holds especially for a temperature load which is constant across the plate thickness ($\overline{T}_0 \neq 0, \quad \overline{\overline{T}}_1 = 0$). No good agreement with the 3D results could be reached for such a loading. In case of a linear temperature distribution $\overline{\overline{T}}_1$, however, the extended 2D values compare quite well in general.

These inconsistencies were thoroughly investigated by Rohwer et al. [16]. They traced them back to lentil-like deformations of each separate layer due to the sinusoidal temperature distribution. Under a temperature load constant through the plate thickness ($\overline{T}_0 \neq 0, \quad \overline{\overline{T}}_1 = 0$) transverse normal stresses are the consequence of inter layer compatibility. In case of a temperature load linearly distributed through the thickness ($\overline{T}_0 = 0, \quad \overline{\overline{T}}_1 \neq 0$) each separated layer would deform either into a concave or convex shape depending on its location in thickness direction. Transverse normal stresses appear as before but with a sign change along x_3. Consequently, the sinusoidal temperature load distribution in x_1 and x_2 will always render transverse normal stresses. The question arises why these stress components are not adequately covered by the extended 2D method.

Equilibrium conditions relate transverse derivatives of the transverse normal stresses to in-plane derivatives of the transverse shear stresses.

$$\sigma_{33,3} = -\sigma_{\alpha 3,\alpha} \tag{29}$$

At the upper and lower plate surface ($x_3 = \pm h/2$) the stresses σ_{33} must vanish. Since they cannot be zero all along x_3 as explained above, non-zero in-plane derivatives of $\sigma_{\alpha 3}$ and therewith these stresses themselves must exist. But they also must vanish at the upper and lower plate surface because of equilibrium conditions.

For a symmetrically stacked plate under a temperature load constant through the thickness ($\overline{T}_0 \neq 0, \quad \overline{T}_1 = 0$) the stresses $\sigma_{\alpha 3}$ must not result in transverse shear forces when integrated over the plate thickness. Consequently the distribution along x_3 must at least have two maximum values. Using now the in-plane equilibrium conditions

$$\sigma_{\alpha 3,3} = \sigma_{(\alpha\alpha),\alpha} + (1 - \delta_{\alpha\beta})\sigma_{(\alpha\beta),\beta} \tag{30}$$

it becomes clear that a linear distribution of in-plane displacements and the resulting piece-wise linear in-plane stresses can not adequately model the structural behavior. A higher order polynomial is necessary. Though these arguments are not fully applicable to plates with non-symmetric stacking or to a linearly distributed temperature load it can be assumed that also in these cases higher order polynomials would lead to a considerable improvement in the transverse shear and normal stress distribution.

3.2.2 Kinematic relations

In order to determine necessary and sufficient polynomial degrees for displacement approximation they are developed into power series in thickness direction.

$$u_\alpha = \sum_{i=0}^{\infty} c_i u_{\alpha_i} \cdot \left(x_3\right)^i \tag{31}$$

$$w = \sum_{i=0}^{\infty} d_i w_i \cdot \left(x_3\right)^i \tag{32}$$

These series must be truncated so that the number of functional degrees of freedom is kept limited. Such approaches have been proposed by several authors. In some cases additional constraints are applied for to further reduce the number of functional degrees of freedom. The applicability of the different theories to thermal loads, however, is seldom checked. The considered sinusoidal temperature distribution, in particular, is treated by Khdeir and Reddy [17]. But their results are restricted to transverse displacements and membrane stresses; transverse stresses are not studied.

In the following, results obtained by means of the extended 2D method based on FSDT will be compared against results with approaches characterized by $c_i = 1$ and $d_i = 1$ for $i = 0,1,2,3$ (HO-3) and for $i = 0,1,2,3,4,5$ (HO-5) whereas higher order terms vanish. For all approaches the standard linear strain displacement relations are assumed. With the polynomial

approximation of the displacements inserted the strains can also be written in the form of a polynomial series.

$$\varepsilon_n = \sum_{i=0}^{\infty} \varepsilon_{n_i} \cdot \left(x_3\right)^i \tag{33}$$

This series is to be truncated according to the truncation of the displacement development.

In general the kinematics described above do not meet the condition of vanishing transverse shear strains at the upper and lower plate surface. These conditions can be utilized to eliminate four functional degrees of freedom. If that is done the corresponding stiffness coefficients must be modified, accordingly, which may impair the quality of the displacement distribution. Furthermore, in case of application in finite elements at least $C^{(1)}$ continuity conditions are required for the shape functions. Since in the following the transverse stresses will be determined by means of the equilibrium conditions zero transverse shear strains at the plate surfaces need not be enforced explicitly in the displacement functions.

3.2.3 Elasticity Relation and Boundary Conditions

Basis for the higher-order theories is the 3D elasticity law of the layer k which in index notation reads

$$_k\sigma_m = {_k}Q_{mn}\left\{\varepsilon_n - {_k}\alpha_n \cdot \Delta T \right\} \tag{34}$$

The stresses can be integrated over the plate thickness leading to stress resultants of the form

$$N_{m_i} = \int_{(h)} \sigma_m \cdot \left(x_3\right)^i dx_3 \tag{35}$$

For $i = 0,1$ these stress resultants are the standard membrane forces and bending/ torsion moments; indices between 2 and 5 point to higher order stress resultants. Correspondingly coefficients of the strain components and the components of the temperature load are to be integrated. To that end the assumed thickness distribution of the strains ε_n and the temperature load ΔT must be inserted. With

$$C_{m_i n_j} = \int_{(h)} Q_{mn} \left(x_3\right)^{i+j} dx_3 \qquad \text{where} \quad i, j = 0,1,2,3,4,5 \text{ for HO-5} \tag{36}$$

and

$$A_{m_i\rho} = \int_{(h)} Q_{mn}\alpha_n \left(x_3\right)^{i+\rho} dx_3 \qquad \text{where} \quad i = 0,1,2,3,4,5 \text{ for HO-5 and } \rho = 0,1 \tag{37}$$

the elasticity relation for the laminated plate reads

$$N_{m_i} = C_{m_i n_j} \varepsilon_{n_j} - A_{m_i\rho} \overline{T}_\rho \tag{38}$$

Therewith equilibrium conditions can be established.

$$N_{11_i},_1 + N_{12_i},_2 - i \cdot N_{13_{i-1}} = 0$$

$$N_{12_i},_1 + N_{22_i},_2 - i \cdot N_{23_{i-1}} = 0 \qquad \text{where} \quad i = 0,1,2,3,4,5 \text{ for HO-5} \qquad (39)$$

$$N_{13_i},_1 + N_{23_i},_2 - i \cdot N_{33_{i-1}} = 0$$

In case of HO-5 these are 18 conditions whereas for HO-3 the number is reduced to 12. Correspondingly there are 2×18 and 2×12 boundary conditions to be satisfied. For a 'simple support' they can be specified as follows:

$$N_{11_i} = u_{2_i} = w_i = 0 \qquad\qquad \text{at} \quad x_1 = 0, L_1 \qquad\qquad (40)$$

$$N_{22_i} = u_{1_i} = w_i = 0 \qquad\qquad \text{at} \quad x_2 = 0, L_2 \qquad\qquad (41)$$

These conditions are met if the displacement functions are of the form

$$\begin{Bmatrix} u_{1_i} \\ u_{2_i} \\ w_i \end{Bmatrix} = \sum_{m=1}^{\infty}\sum_{n=1}^{\infty} \begin{Bmatrix} (\bar{u}_{1_i})_{mn} \cos(m\pi x_1/L_1) \quad \sin(n\pi x_2/L_2) \\ (\bar{u}_{2_i})_{mn} \sin(m\pi x_1/L_1) \quad \cos(n\pi x_2/L_2) \\ (\bar{w}_i)_{mn} \sin(m\pi x_1/L_1) \quad \sin(n\pi x_2/L_2) \end{Bmatrix} \qquad (42)$$

3.2.4 Transverse Stresses

The applied temperature load consists of the first term of the Fourier series only. Thus it is sufficient to restrict the displacement functions likewise. Inserting these displacement functions into the strain displacement relation and using the resulting strains together with the stiffness coefficients and the temperature load in the equilibrium conditions yields a set of linear algebraic equations for to determine the unknown coefficients $\bar{u}_{\alpha_i}$ and $\bar{w}_i$. They fully specify the displacements.

For the determination of the transverse stresses, only the membrane displacements u_{α_i} are used. In-plane derivatives are formed to derive at the membrane strains. With the aid of the material law the membrane stresses are calculated for each layer. By means of the local equilibrium conditions the in-plane derivatives of the membrane stresses are integrated to get the transverse shear stresses, whereas integrating the in-plane derivatives of these transverse shear stresses results in the transverse normal stresses.

3.2.5 Numerical Application

By means of two examples the effects discussed above are evaluated. Results obtained with the extended 2D method (FSDT), with a cubic (HO-3) and with a fifth order (HO-5) displacement approximation are compared against analytical 3D solutions. Plates with two different lay-ups are analysed, a four layer anti-symmetric stacking of [0,90,0,90], and a ten-layer symmetric stacking [0,90,0,90,0]$_S$. The plates are of quadratic ground shape with a slenderness ratio of s=L/h=5. This rather small ratio is chosen to make the differences between the theories more visible.

Material properties and loading conditions are as specified in equation (27). Transverse shear stresses σ_{13} and σ_{23} are determined at the mid-side edge points $(0;L_2/2)$ and $(L_1/2;0)$, respectively, whereas the transverse normal stresses σ_{33} are calculated at the plate center $(L_1/2;L_2/2)$. Due to the applied thermal load and the boundary conditions these are the points where the stresses reach maximum values. The stress distribution in x_1- and x_2-direction follows harmonic functions.

Transverse shear and normal stresses in the [0,90,0,90] laminate are depicted in Figure 21. Such a lay-up leads to a bending deformation even for the constant thermal load ($\overline{T}_0 \neq 0, \quad \overline{T}_1 = 0$). Transverse shear forces must develop at the edges. That is reflected by the transverse shear stresses σ_{13} and σ_{23}. Their zig-zagging mode can be explained by abrupt stiffness changes between the 0°- and the 90°-layers. Values of σ_{13} and σ_{23} are of opposite sign but exactly central symmetric in magnitude. Transverse normal stresses σ_{33} are compressive at the plate center. That again is due to compatibility constraints in connection with the lentil-like deformations.

With the extended 2D method (FSDT) the zig-zagging modes of the transverse shear stresses are well captured. Though the values are somewhat off they still show exact central symmetry. The transverse normal stresses, however, are determined as tensile, their distribution differs drastically from the 3D results. Cubic and fifth order displacement approximations deliver transverse stresses which are nearly identical to the 3D solution.

Through linearly distributed thermal loads ($\overline{T}_0 = 0, \quad \overline{T}_1 \neq 0$) additional bending is induced. Figure 21 shows that it results in transverse shear stresses which are of opposite sign in the upper and lower half of the plate. The distribution of σ_{13} in positive x_3-direction is exactly the same as that of σ_{23} in negative x_3-direction. Transverse normal stresses σ_{33} are rather small with tensile values in the upper half and compressive ones in the lower half. The relatively small contribution due to the compatibility constraints of concave and convex deformation shapes of separated slices must be superimposed by larger transverse normal stresses due to bending.

Distribution shapes of transverse shear and normal stresses are rather well captured by the extended 2D method (FSDT). Maximum values of the normal stresses, however, exceed those of the 3D results by about 25%. Results of the cubic displacement approximation are much more accurate, and the fifth order approach show hardly any difference to the exact solution.

Results obtained for the [0,90,0,90,0]$_S$ plate are summarised in Figure 22. Constant temperature through the thickness ($\overline{T}_0 \neq 0, \quad \overline{T}_1 = 0$) leaves the symmetry plane straight but the sinusoidal distribution in x_1 and x_2 causes lentil-like deformation as mentioned above. Each layer undergoes bending deformation, and because of the abrupt stiffness changes between the 0°- and the 90°-layers transverse shear stresses appear in a zig-zagging mode. Distribution through the thickness of σ_{13} as well as of σ_{23} is exactly central symmetric. At the plate center compressive normal stresses σ_{33} appear due to inter layer compatibility.

Again, the extended 2D method (FSDT) captures the central symmetric zig-zagging shape of the transverse shear stresses quite well, though the values, especially for σ_{13}, are somewhat off. But the transverse normal stresses are in no way comparable with the exact results. Cubic

and fifth order approximation result in transverse shear stresses which hardly deviate from the 3D solution. For σ_{33} the cubic approximation yields a maximum value at the plate center which is 7.1% too large, whereas the fifth order approximation result is again very close to the 3D value.

Under a linear temperature distribution ($\overline{T}_0 = 0, \quad \overline{T}_1 \neq 0$) the bending deformation result in positive values for σ_{13} and corresponding negative values for σ_{23}. With exception of the two central 0°-layers it are again zig-zagging forms, but now symmetric with respect to the center plain. Again, transverse normal stresses are rather small, with compressive values in the upper half and tensile ones in the lower half. They can be explained by the compatibility constraints of concave and convex deformation shapes due to positive and negative temperature difference, respectively.

Especially the shear stresses σ_{13} is quite well modelled by the extended 2D method (FSDT), σ_{23} is much worse. That is because of the larger membrane and bending stiffness in x_1-direction as compared to x_2. The transverse normal stresses by the extended 2D method capture only the bending effect, not the lentil-like deformations and is therefore no way near the exact results. The cubic approximation (HO-3) delivers rather accurate transverse shear stresses, whereas the normal stresses are 33% too large at the maximum. All results from the fifth order approximation compare very well with the exact results.

The examples clearly point out that a variation in temperature difference over the reference surface results in effects which cannot be captured by the FSDT. That holds especially for the transverse normal stresses. Though their absolute values are relatively small they should not be neglected since the corresponding strength in layered composites is also rather small. Therefore, in case of a temperature load with considerable gradients in the in-plane direction the application of higher order theories (HO-3 or HO-5) is strongly recommended.

3.3 Thermally Induced Buckling

In aircraft and reentry vehicle structures there are many structural components which, caused by its high slenderness and predominant in-plane loading, are prone to fail by loss of stability at a load which is significantly below the strength limit. Thus, after having calculated the temperature field (cf. chapter 2) and having checked the strength by use of thermal stress and failure analysis (cf. chapter 3.1 and 3.2) the stability behaviour under combined thermo-mechanical loading must be investigated.

The thermal buckling of laminated composite plates and shells has been investigated by several authors (e.g. [18], [19], [20], [21], [22]), none of which however considered design rules for thermo-mechanical buckling of stringer stiffend panels. This is done subsequently by the example of a flat stiffened panel. Previously, finite element modelling philosophy and test correlation are discussed by the example of a curved, so-called validation panel, which might be representative for a fuselage structure. The content is primarily based on the work reported in [23, 24, 25].

In order to establish a validated finite element model a panel designed for global buckling (conf. Figure 23) was tested and analyzed. It had a length of 800 mm, a radius of 400 mm and an arc length of 420 mm. It was stiffened by six blade-stringers of 14 mm height. The stacking sequence of the skin was $[(+45/-45)_2 / 90 / 0]_s$ which yielded a thickness of 1.5 mm. The temperature dependent material properties of Fiberite 954-2A/IM7 are given in table 1. The panel was tested within the THERMEX-B facility of EXSACOM [26]. This test site is equipped with segmented clamping boxes at both sides which allow for transverse expansion of the test panel (y-direction). Furthermore the unloaded straight edges of the panel are fixed between two buckling supports each in order to prevent wrinkling. It turned out that very precise modeling of these boundary conditions is of major importance for realistic representation of the buckling behavior. A first approach to model the buckling supports was the assumption w=0. This resulted in a very stiff structure, because the panel behaved like being fixed in a stiff frame. The problem was solved by coupling the rotational degrees of freedom of the nodes in the region of the buckling support. By that means the straight edges acted like rigid structures which could perform any rigid body movement (conf. Fig. 23). The areas of the FE-model with boundary conditions reflecting the clamping (curved edges) were changed in their length, and a separate coordinate system was defined to allow transverse deformations δv.

Another important modeling aspect concerns the eccentricity of the foot of the blade stringers. Modeling the foot as local stiffening of the skin with unmodified reference plane is presumably an efficient method which introduces only a minor inaccuracy. However, computational results reveal an important influence on the buckling behavior. Thus, the exact eccentricity must be taken into account, e.g. by modeling skin and foot with separate shell elements and connecting them by beam elements. Two nominally identical panels were tested. The first one was subjected to pure mechanical loading under room temperature until buckling. The global buckling pattern yielded damaging of the panel. Thus the second panel was treated up to 150°C on the outside and, after having reached steady state, was compressed until buckling. The temperature distribution was calculated by finite elements and transferred to the buckling analysis model. Finally, a nonlinear buckling computation taking into account temperature dependent material properties and initial imperfections in the form of the first eigenmode (with amplitude δ_z=0.1 mm) was carried out. An adequate choice of imperfections was crucial for the curved panel. A too small imperfection did not affect the buckling at all, whereas a too big one dominated the behavior. Table 2 shows the favorable agreement

between calculation and experiment for both tests. In Figure 24 a very good comparison of buckling patterns can be seen. It is worthwhile to notice that the additional thermal loading did not have a significant influence on the buckling load. This was more thoroughly investigated by further computations.

For this purpose flat stringer-stiffened panels were selected. Firstly, they are typical for wings of supersonic aircraft, the curvature of which is negligible. Secondly, they exhibit a postbuckling behavior which is quite different from curved panels. The latter resulted in a very low sensitivity with respect to geometrical imperfections. Different amplitudes for imperfections in the form of first and second buckling modes (conf. Figure 25b/c) were numerically tested but did not have a significant effect. The same finite element modeling philosophy was used as for the curved validation panel. The panel depicted in Figure 25a with $(\pm 45, 0)_s$ - and $(\pm 45, 0_3)_s$ - lay-ups for skin and stringer, respectively and made from CIBA 6376/HTA (temperature dependent material properties are given in [25]) was subjected to combined thermal and mechanical loading. The design resulted from an optimization for buckling load maximization. The linear buckling load under pure mechanical loading of 93.3 kN was basically not reduced by simultaneous heating within a realistic range up to 150°C. This result was confirmed by geometrically and physically non-linear computations which provided identical load-shortening curves for 25°C and 100°C. Again, like in the previous investigation of the curved panel, the transverse expansion was unrestrained. In the next step the unloaded edges (parallel to the stringers) were fixed in transverse and normal direction (v = w = 0) whereas the rotations were left unrestrained. These boundary conditions might be close to those of wing panels fixed to ribs and spars. Figure 26 shows that the buckling load under pure mechanical load is less than half of the value obtained before. Furthermore, a very pronounced reduction of the buckling load due to temperature increase could be observed. The transverse expansion of the skin laminate is rather high under mechanical and thermal loading. In order to reveal this influence two extreme designs were investigated. 0° plies only in the skin result in maximum transverse expansion and yielded a rather high mechanical bifurcation load of 85.3 kN, whereas the critical buckling temperature difference was only 18.5°C (conf. table 3). Consequently, pure 90° plies in the skin provided a lower bifurcation load (60.6 kN) and a higher critical temperature (115.6 °C). An optimisation for maximum mechanical buckling load at room temperature resulted in a $(90 / 0)_s$ design with a bifurcation load of 86.3 kN. Also the critical temperature difference of 88.6 °C was rather high in this case.

Summarizing the thermal buckling investigation of stiffened panels it can be stated that possibility to expand transverse to the loading direction has a decisive influence on the optimum structural design and on the effect of additional thermal loading. Thus, the designer has to make sure that the boundary conditions of the panel to the surrounding structure are modeled precisely. Then, independent of the boundary conditions chosen, an optimization for maximum mechanical buckling load is also appropriate for additional thermal loading. When modeling panels with finite elements not only the boundary conditions but also the connection between stringers, stringer foot and skin must be represented accurately, especially representing eccentricities correctly.

References

[1]   J. Argyris, L. Tenek and F. Öberg, A Multilayer Composite Triangular Element for Steady – State Conduction/Convection/Radiation Heat Transfer in Complex Shells, Computer Methods in Applied Mechanics and Engineering, vol. 120, pp. 271-301, 1995.

[2]   R. Rolfes, Efficient Thermal Analysis of Anisotropic Composite Plates Using New Finite Elements, in: Füller, J.; Grüninger, G.; Schulte, K.; Bunsell, A.R.; Massiah, A.: Developments in the Science and Technology of Composite Materials, Proceedings of the Fourth European Conference on Composite Materials (ECCM4), Stuttgart, pp. 743-748, 1990.

[3]   J. Noack and R. Rolfes, Efficient thermal analysis of hot structures using new finite elements, Proceedings European Conference on Spacecraft Structure, Materials and Mechanical Testing, Braunschweig, Germany, pp. 117-120, 1998.

[4]   J. Noack, Eine schichtweise Theorie und Numerik für Wärmeleitung in Hybridstrukturen, Dissertation, FB Maschinenbau, TU Braunschweig, Shaker Verlag, Aachen, 2000.

[5]   A. K. Noor and W. S. Burton,Steady-State Heat Conduction in Multilayered Composite Plates and Shells, Computers & Structures, vol. 39, pp. 185-193, 1991.

[6]   J. N. Reddy, A Simple Higher-Order Theory for Laminated Composite Plates, Journal of Applied Mechanics, vol. 51, pp. 745-752, 1984.

[7]   R. Rolfes, Higher Order Theory and Finite Element for Heat Conduction in Composites, in: R. W. Lewis ,J. H. Chin and G. M. Homsy (ed), Numerical Methods in Thermal Problems, Proceedings of the Seventh International Conference, vol. VII, pp. 880-889, 1991.

[8]   R. Rolfes, J. Noack and M. Taeschner, High performance 3D-analysis of thermo-mechanically loaded composite structures, Composite Structures, vol. 46, pp. 367-379, 1999.

[9]   V. S. Sipetov, V. S. Karpilovskii and O. N. Demchuk, Application of the Finite Element Method to Solve the Stationary Heat Conduction Problem of Piecewise Inhomogeneous Systems, J. Eng. Phys. 55, Nr. 6, pp. 1439-1443, 1989.

[10]   W. C. Swinbank, Long-wave radiation from clear skies, Quarterly J. of Royal Meteorol. Society, vol. 89, pp. 339-348,1963.

[11]   R. H. B. Exell, Atmospheric Radiation, http://www.jgsee.kmutt.ac.th/exell/Solar/atmosph.html, 2003.

[12]   A. Puck, Festigkeitsanalyse von Faser-Matrix-Laminaten, Modelle für die Praxis Carl Hanser Verlag, München, Wien, 1996.

[13]   C.W. Pryor and R.M. Barker, A Finite Element Analysis Including Transverse Shear Effects for Application to Laminated Plates, AIAA Journal, vol. 9, pp. 912-917, 1971.

[14]   R. Rolfes, K. Rohwer and M. Ballerstaedt, Efficient Linear Transverse Normal Stress Analysis of Layered Composite Plates, Computers and Structures, vol. 68, pp. 643-652, 1998.

[15]   R. Rolfes, A. K. Noor and H. Sparr, Evaluation of Transverse Thermal Stresses in Composite Plates Based on First-Order Shear Deformation Theory, Computer Methods in Applied Mechanics and Engineering, vol.167, pp. 355-368. 1998.

[16]   K. Rohwer, R. Rolfes and H. Sparr, Higher-Order Theories for Thermal Stresses in Layered Plates, International J. of Solids and Structures, vol. 38, pp. 3673-3687, 2001.

[17]   A. A. Khdeir and J. N. Reddy, Thermal Stresses and Deflections of Cross-Ply Laminated Plates Using Refined Plate Theories, J. of Thermal Stresses, vol. 14, pp. 419-438, 1991.

[18] L.X. Sun and T.R. Hsu, Thermal buckling of laminated composite plates with transverse shear deformation, Computers and Structures, vol. 36, pp. 883-889, 1990.

[19] A.K. Noor, Thermomechanical buckling and postbuckling of multilayered composite panels, AIAA Paper 92-2541.

[20] K. Rohwer, A further study on thermal buckling of simply supported antimetric angle-ply laminates in a uniform-temperature field, Composite Science and Technology, vol.46, no.1, pp. 85-86,1993.

[21] A.K. Noor and W.S. Burton, Three-dimensional solutions for the thermal buckling and sensitivity derivates of temperature-sensitive multilayered angle-ply plates, Transaction J. of Applied Mechanics, vol.59, no.4, pp. 848-856, 1992.

[22] C.A. Meyers and M.W. Hyer, Thermal buckling of symmetrically laminated composite plates, Mechanics of composites at elevated and cryogenic temperatures Proc. Symposium, ASME Applied Mechanics Conf., Columbus, OH June 16-19 1991; NY, ASME, pp. 287-303, 1991.

[23] R. Rolfes, S. Tacke and R. Zimmermann, Development and Experimental Verification of FE-Model for Stringer-Stiffened Fibre Composite Panels under Combined Thermal and Mechanical Loading Conditions, Proceedings European Conference on Spacecraft Structures, Materials, and Mechanical Testing, 4.-6. November 1998, Braunschweig, ESA SP-428, pp. 109-115., 1999.

[24] D. Petersen,R. Rolfes, J. Noack and B. Hildebrandt, Thermo-Mechanical Behaviour of Large Transport Aircraft Structures, Proceedings ODAS 99 (ONERA-DLR Aerospace Symposium), 21.-24. Juni 1999, Paris, 1999.

[25] D. Petersen, R. Rolfes and R. Zimmermann, Thermo-Mechanical Design Aspects for Primary Composite Structures of Large Transport Aircraft, Aerospace Science and Technology, vol. 5, pp. 135-146, 2001.

[26] www.exsacom.de, homepage of the major EU research infrastructure EXSACOM (Experimental Structural Analysis of Advanced Composites)

Figures
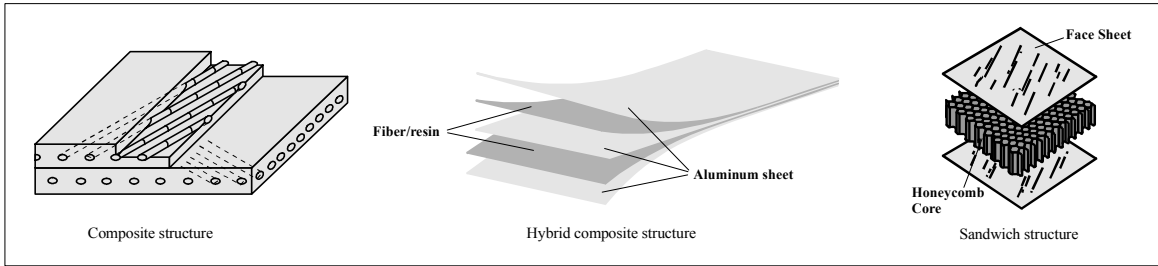
Figure 1: Examples of different composite structures
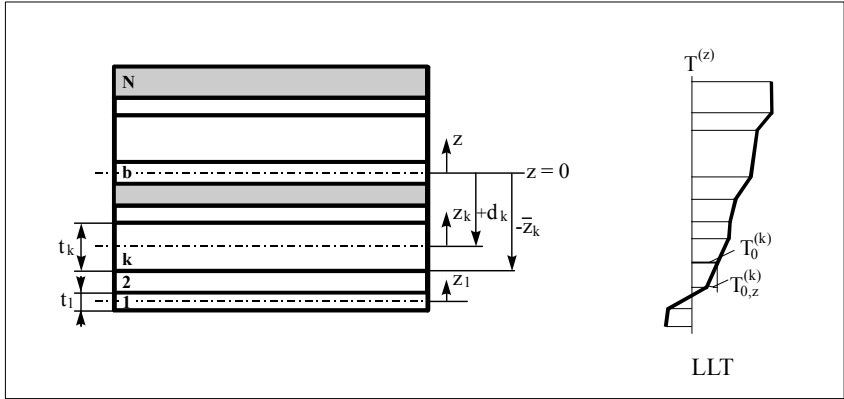
Figure 2: Layered design of composite and sandwich structures
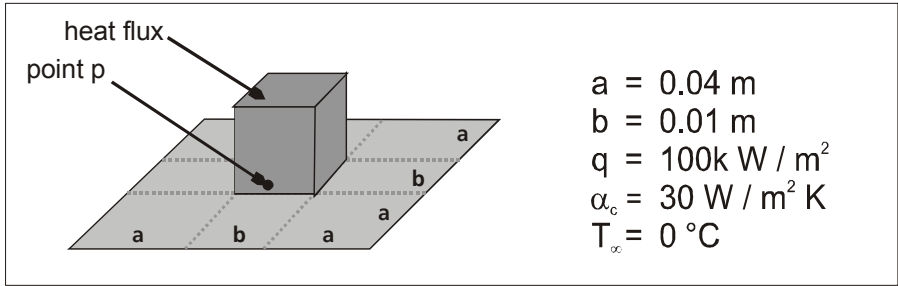
Figure 3: Example problem for the thermal analysis
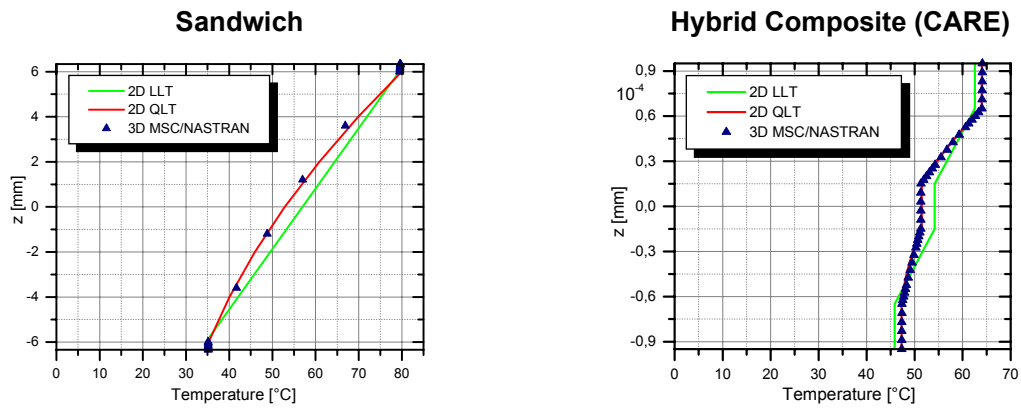
Figure 4: Comparison of 2D and 3D thermal analysis (transverse temperature distribution at point P)
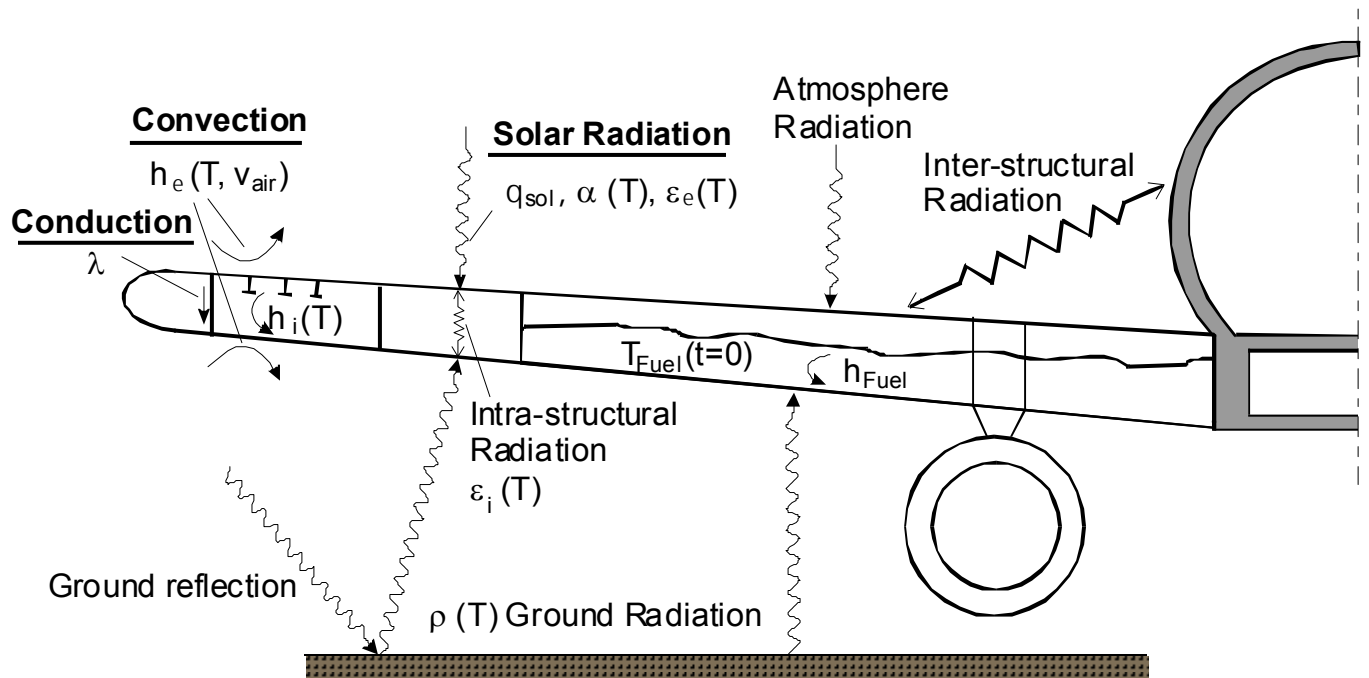
Figure 5: Environmental heat transfer process with aircraft structure
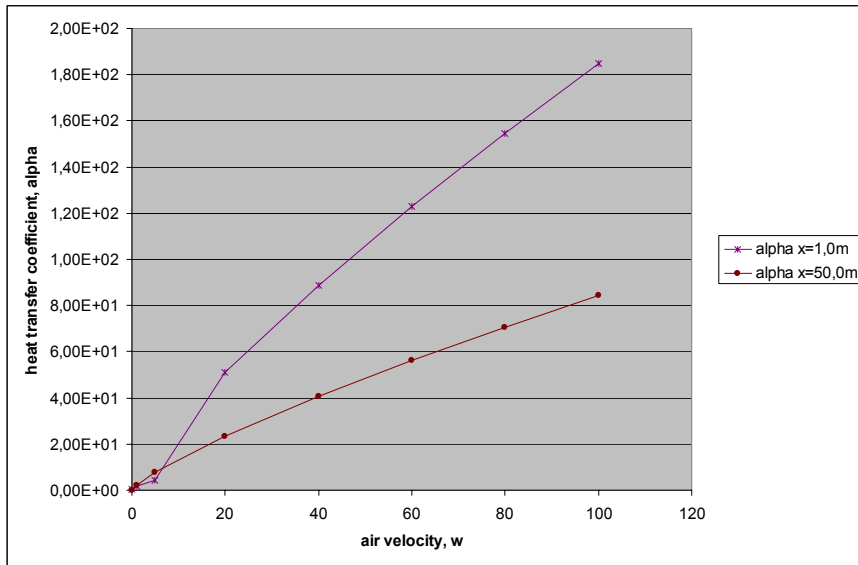
Figure 6: Heat transfer coefficient for two different positions
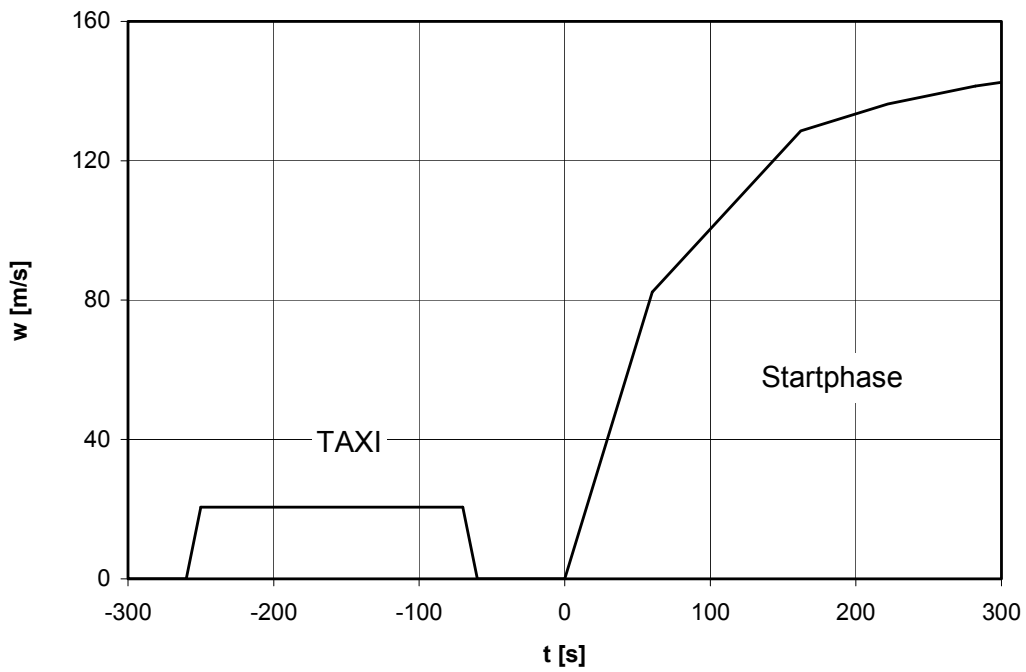
Figure 7: Air flow velocity for take off scenario
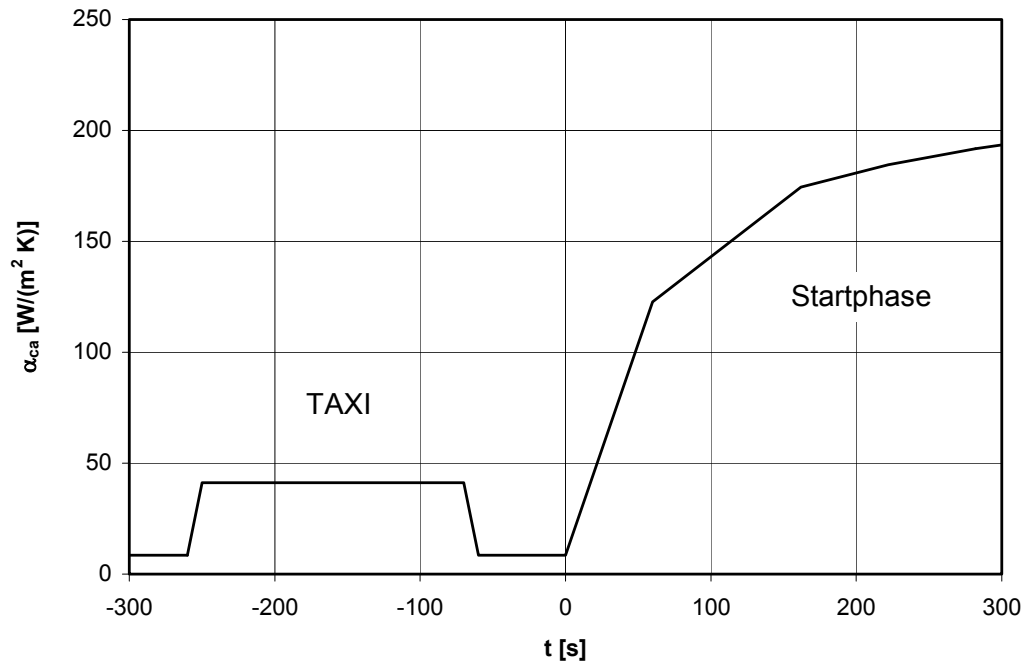
Figure 8: Heat transfer coefficient
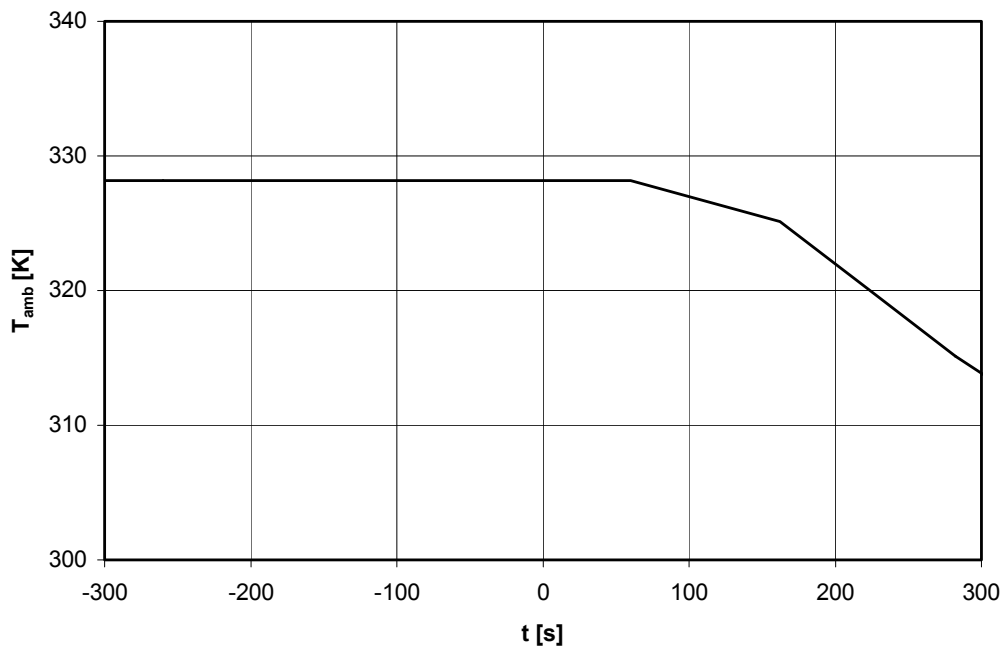
Figure 9: Ambient air temperature for take off scenario

Figure 10: CFRP wing box

oha - upper skin outside

ohi - upper skin inside

uha - lower skin outside

uhi - lower skin inside

ostr - upper skin at stringer

ustr - lower skin at stringer
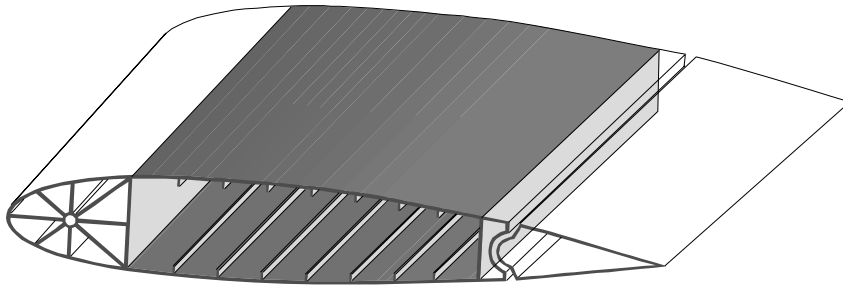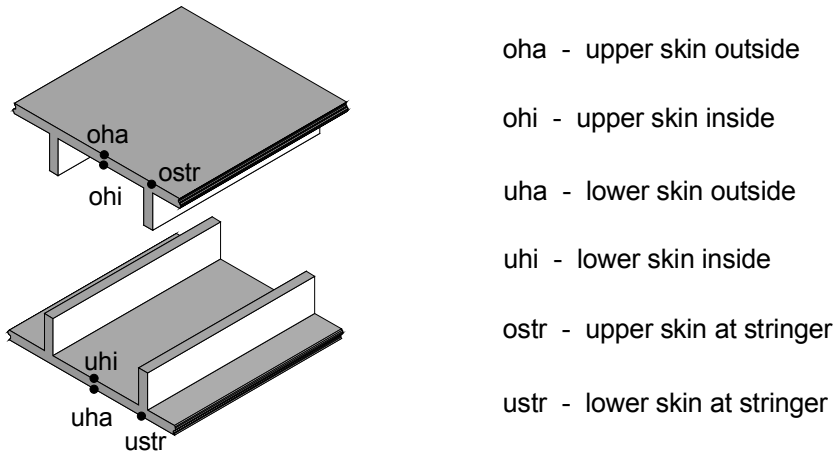
Figure 11: Evaluation points for thermal analysis of wing box
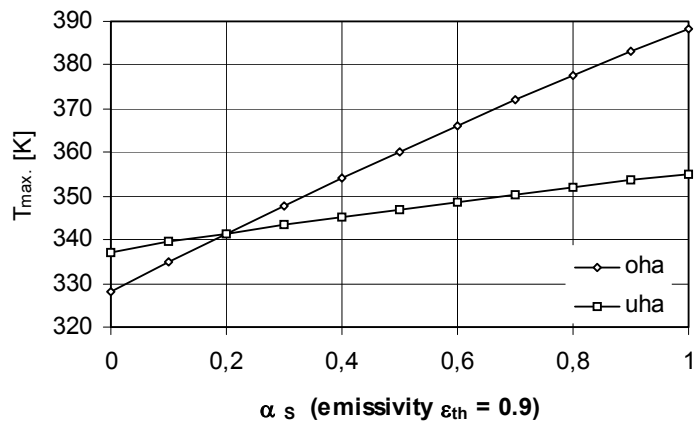
Figure 12: Steady state temperature for varying solar absorption coefficient
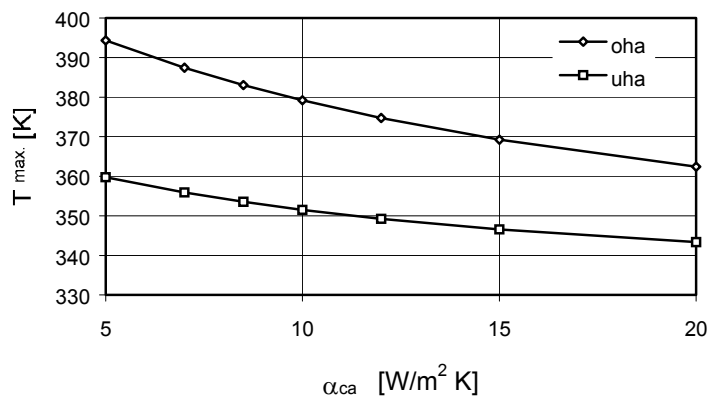
Figure 13: Steady state temperature for varying heat convection factor
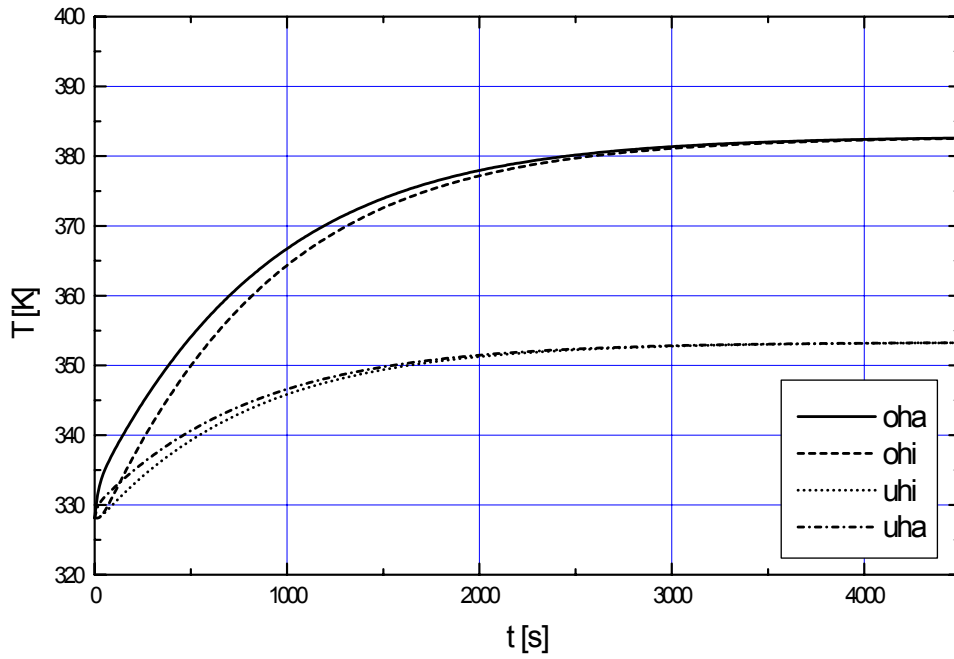
Figure 14: Heating of wing box under hot conditions
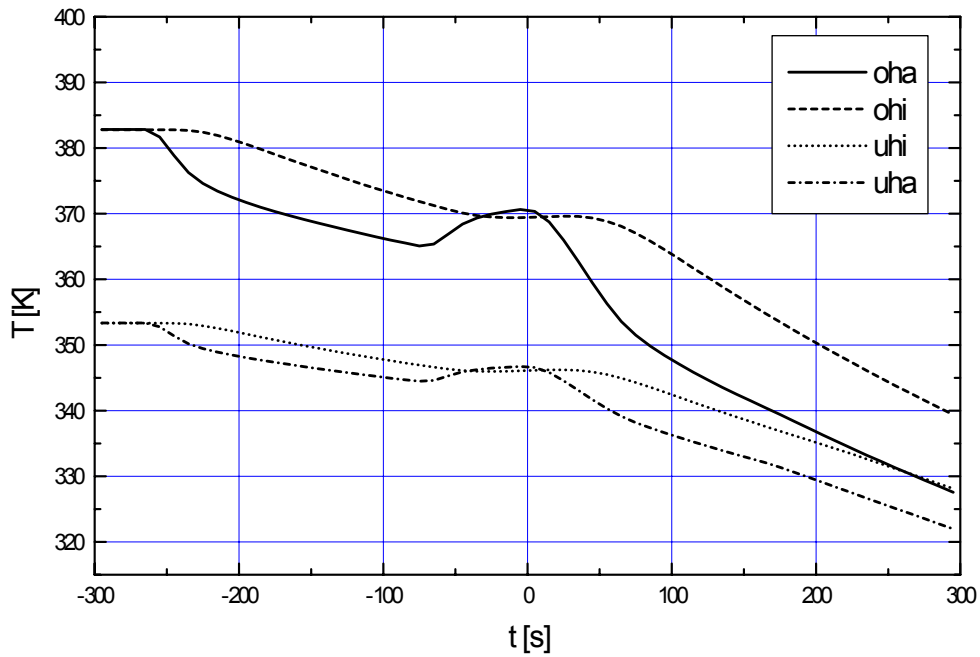
Figure 15: Transient cooling of wing box during take off scenario
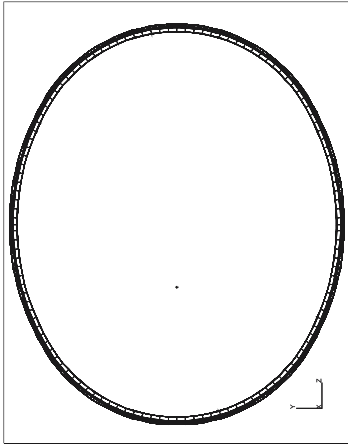
Figure 16: Fuselage cross section
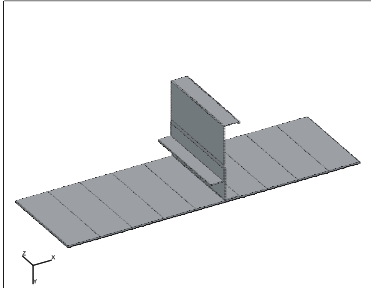
Figure 17: Panel of fuselage
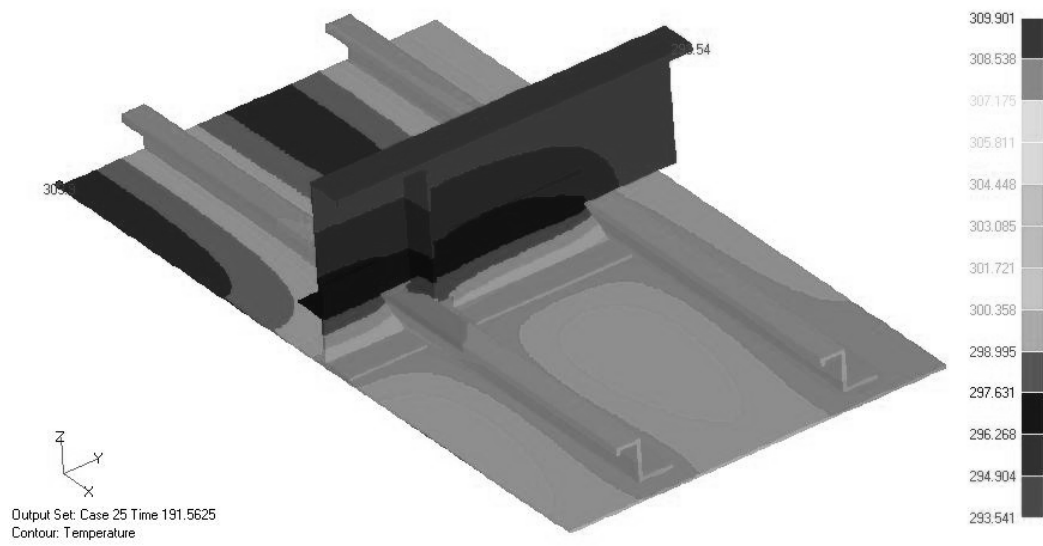
Figure 18: Temperature field of panel during heating
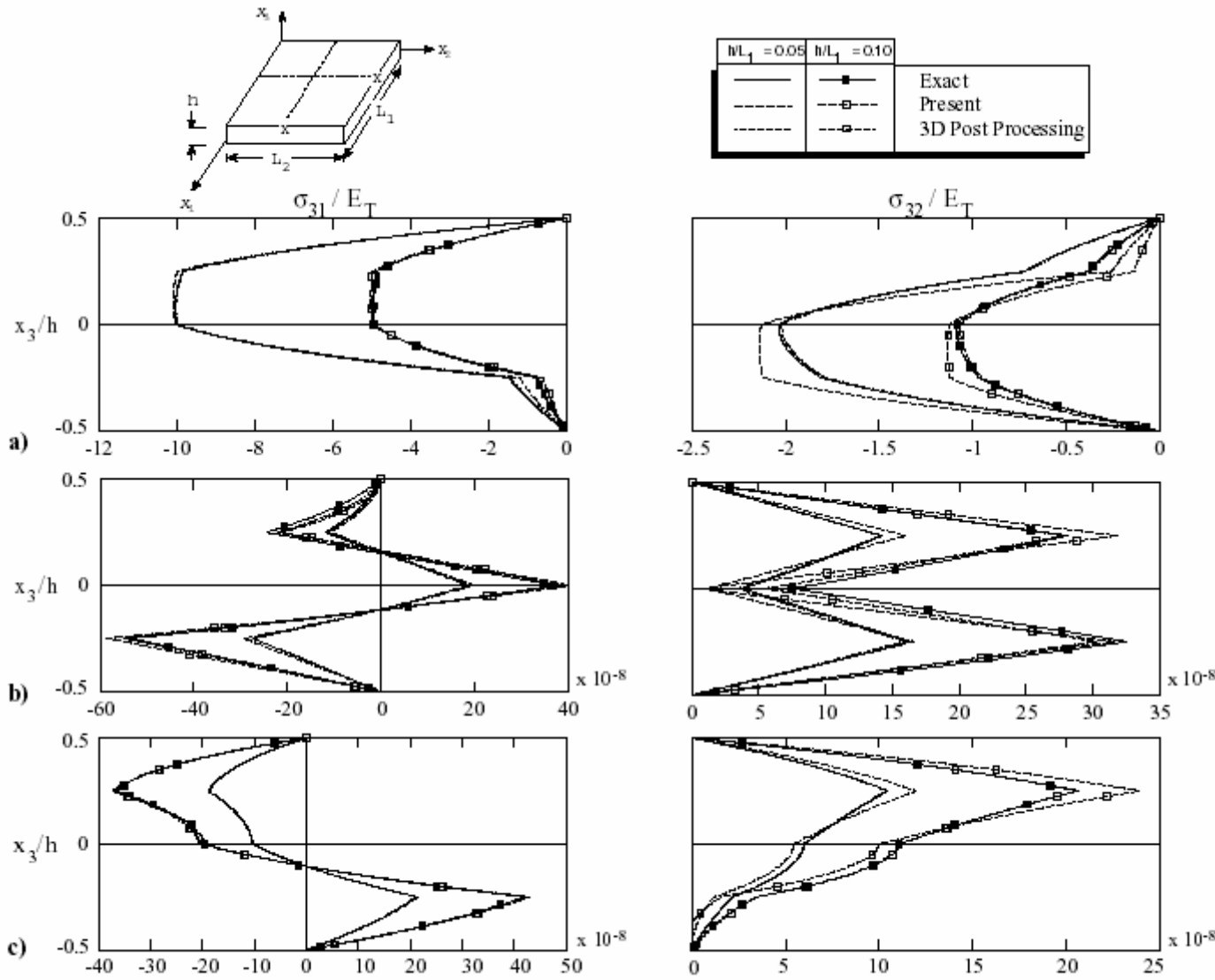
Figure 19: Through-the-thickness distributions of transverse shear stresses (σ_{31} at L_1, $L_2/2$); σ_{32} at $L_1/2$, L_2)). Four-layer antisymmetric cross-ply laminate with $L_2/L_1 = 2$ subjected to: (a) static loading p; (b) uniform temperature T^0; (c) temperature gradient T^1.
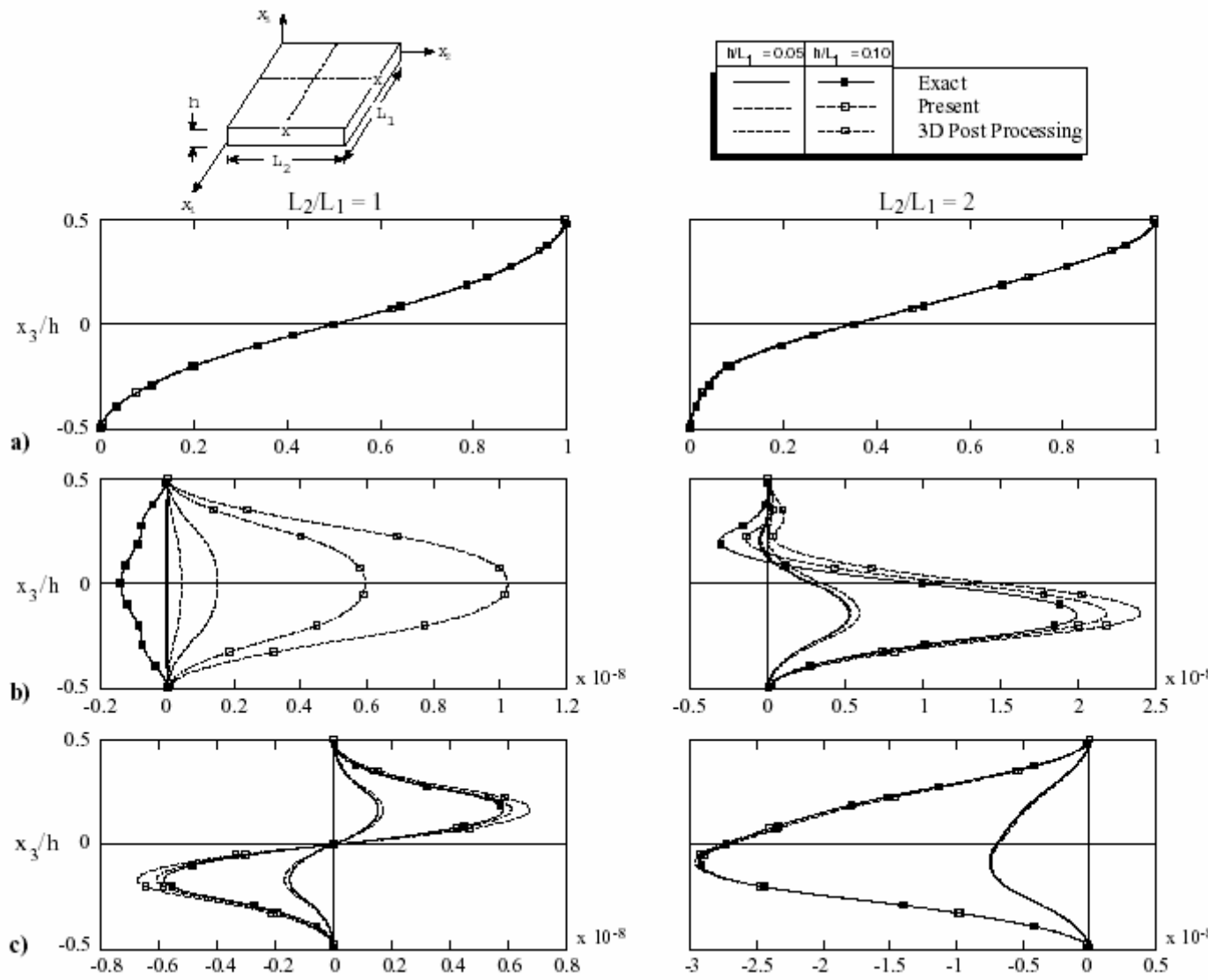
Figure 20: Through-the-thickness distribution of transverse normal stress σ_{33} at $(L_1/2, L_2/2)$. Four-layer antisymmetric cross-ply laminate subjected to: (a) static loading p; (b) uniform temperature T^0; (c) temperature gradient T^1.
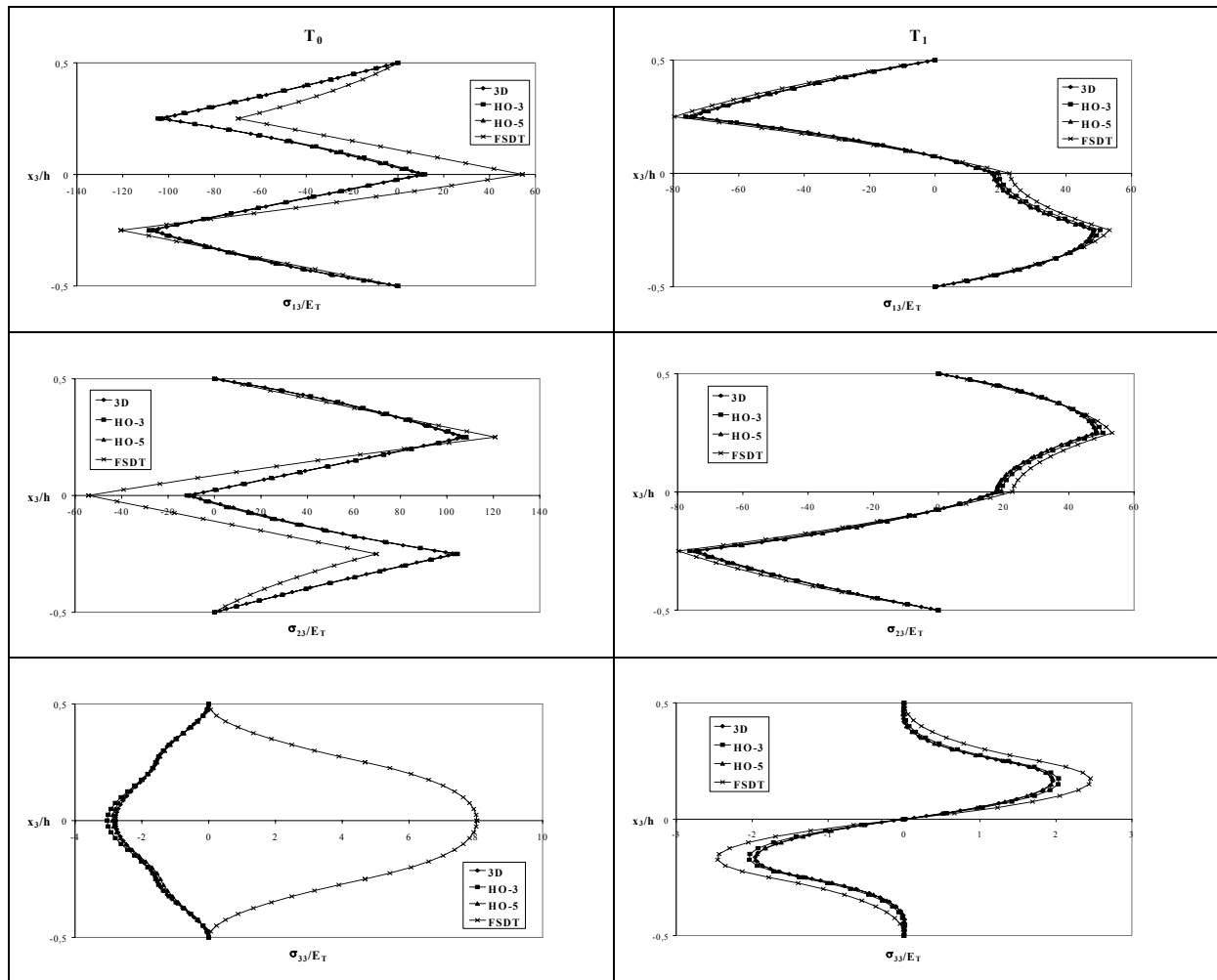
Figure 21: Transverse Stresses in an Anti-Symmetric [0,90,0,90] Plate
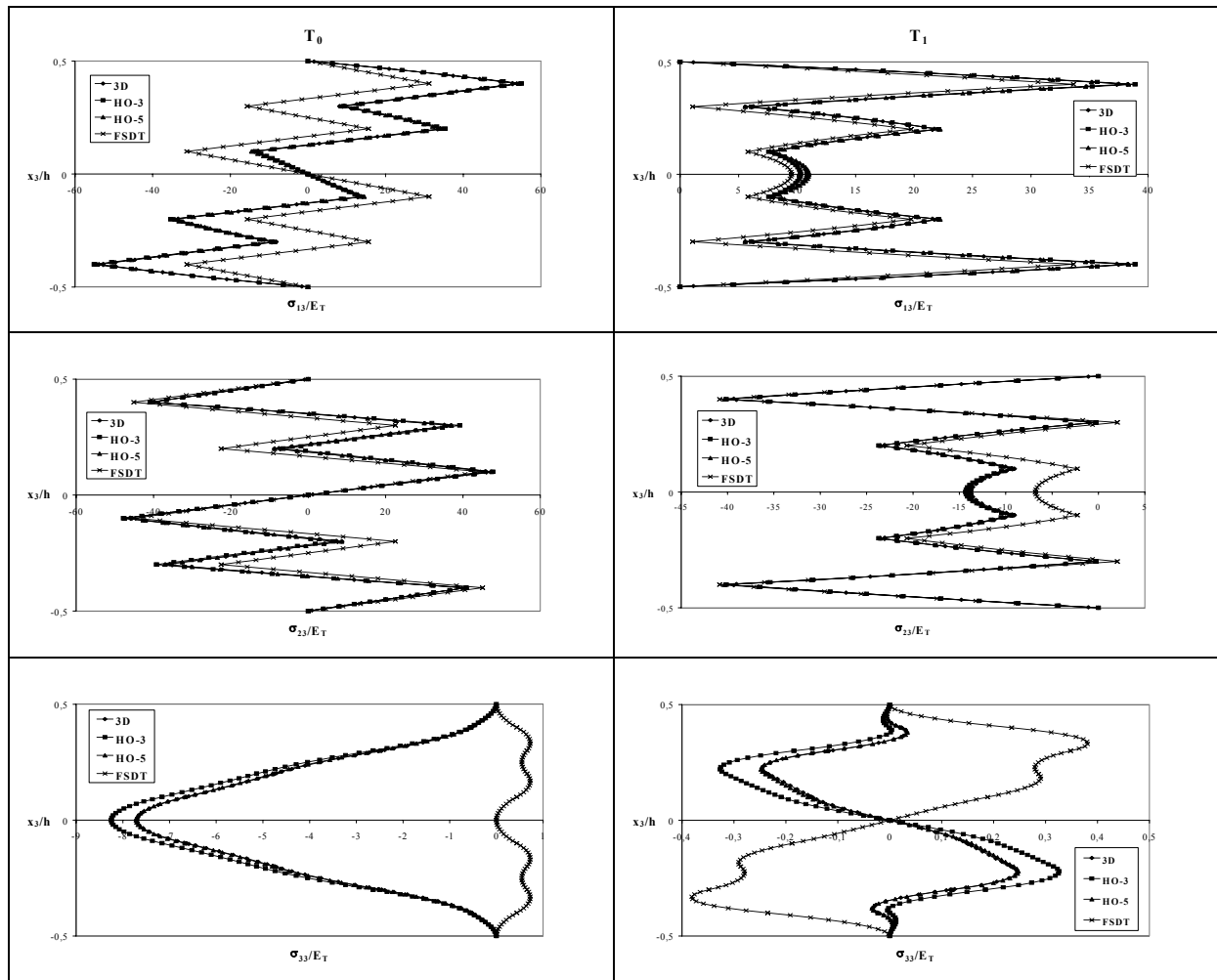
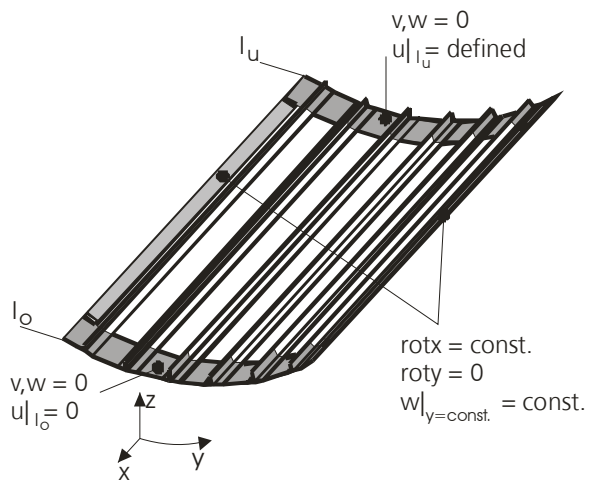Figure 22: Transverse Stresses in a Symmetric [0,90,0,90,0]$_S$ Plate

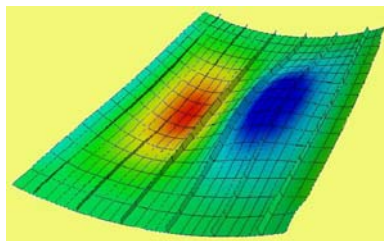Figure 23: Sketch of panel co-ordinate system and boundary conditions
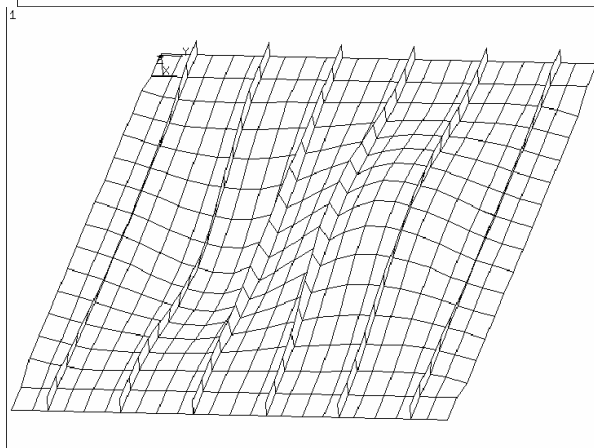

Fig. 24:Experimental and calculated buckling mode

z

y

x

u = defined

conf.
right
boundary

rot x = const.
rot y = 0
$u/_{y=const.}$ = const.

a

w = 0; w,x = w,y = 0   u = 0
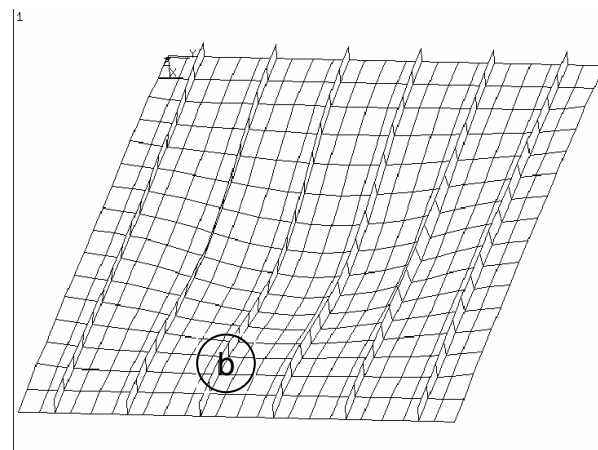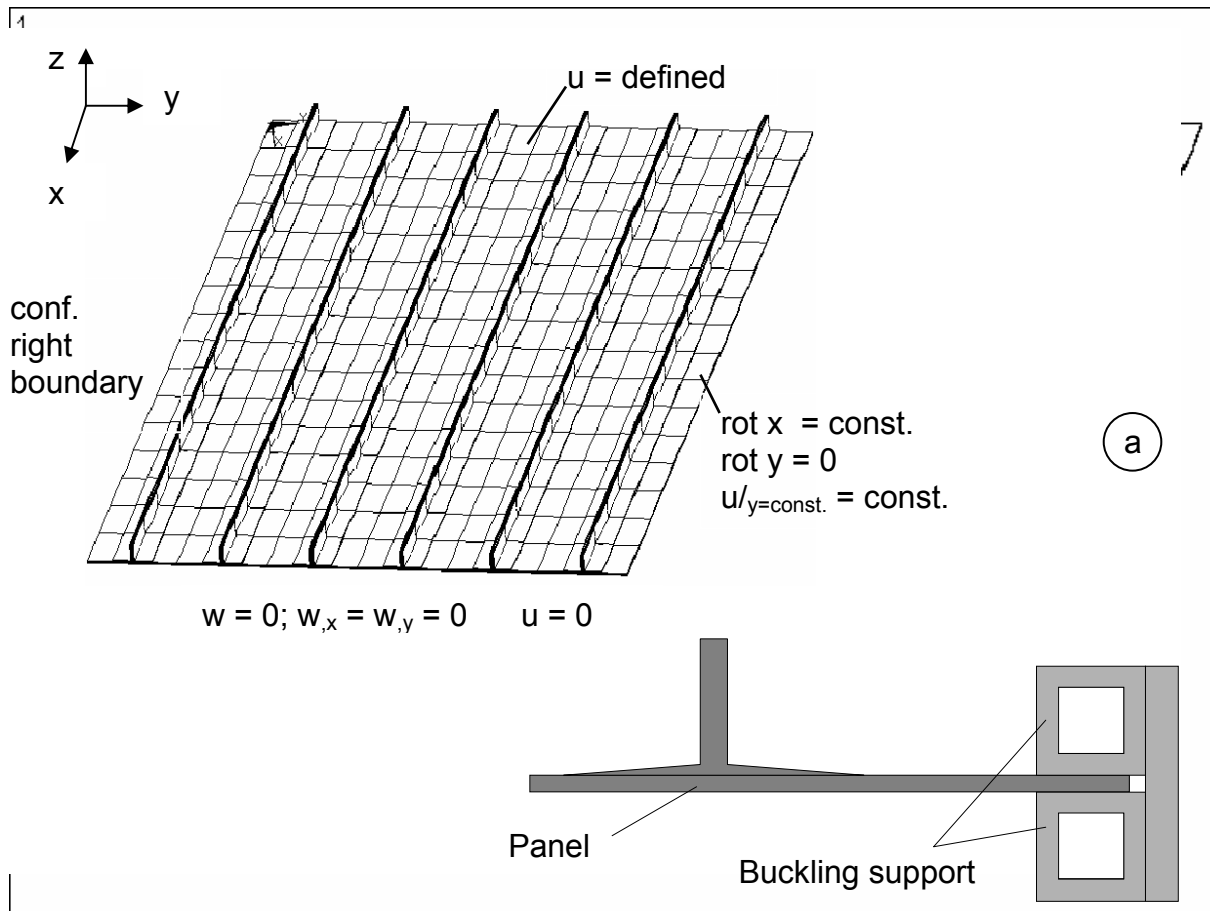
Panel

Buckling support

b

c

Figure 25:   Flat panel with six stringers for investigation of imperfection sensitivity
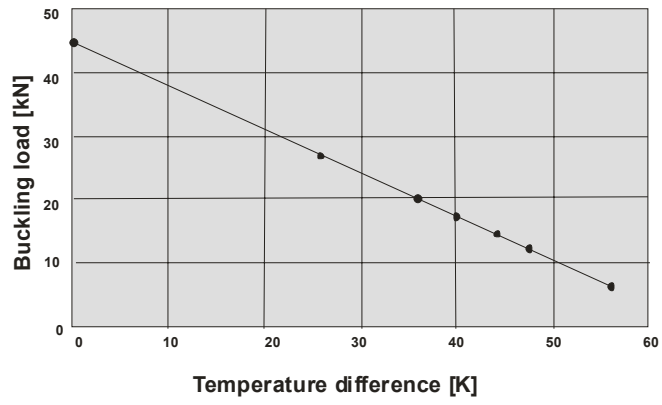
Figure 26: Critical axial force – temperature difference diagram of linear bifurcation computations of panel with fixed unloaded edges

Tables

Table 1: Material properties of Fiberite 954-2A/IM7

	Room temperature	150 °C
$E_{11,t}$	156 GPa	166 GPa
$E_{22,t}$	9.2 GPa	7.4 GPa
$E_{11,c}$	155 GPa	160 GPa
$E_{22,c}$	9 GPa	not obtained
ν_{12}	0.34	0.30

Table 2: Comparison of buckling loads

	Calculation	Experiment
Pure mechanical load	208.30 (linear) 185.22 (nonlinear)	182.0
Additional thermal load 1	185.23 (nonlinear)	175.8

Table 3: Mechanical bifurcation buckling loads and critical temperature differences for variations of skin lay-up

Panel skin-layup	1 Mechanical bifurcation load [kN]	1.1.1 Critical temperature difference [K]
0°	85.3	18.50
90°	60.6	115.59
(90°, 0°)$_s$	86.3	88.625